FACULTY
OF MATHEMATICS
AND PHYSICS
Charles University

DOCTORAL THESIS

Alexander Pitňa

Turbulence in the solar wind from inertial to kinetic scales

Physics of Plasma and Ionized Media

Supervisor of the doctoral thesis: Prof. RNDr. Jana Šafránková, DrSc.

Study programme: Physics

Study branch: 4F2

Prague 2019

I declare that I carried out this doctoral thesis independently, and only with the cited sources, literature and other professional sources.

I understand that my work relates to the rights and obligations under the Act No. 121/2000 Sb., the Copyright Act, as amended, in particular the fact that the Charles University has the right to conclude a license agreement on the use of this work as a school work pursuant to Section 60 subsection 1 of the Copyright Act.

In ..... date ..... signature of the author

I dedicate this thesis to my beloved daughters, Viky and Andy. I am grateful to my wife Barbora Pitňa Lásková and my mother for their love and support during my studies. I would like to express my gratitude to my advisor Prof. RNDr. Jana Šafránková, DrSc. and Prof. RNDr. Zdeněk Němeček, DrSc., for their kindness and sustained support. Furthermore, I would like to thank to my friends for fruitful discussions, Luca Franci, Gilbert Pi, Victor Montagud Camps, Tereza Ďurovcová, Jakub Enžl, to name a few. Finally, I would express gratitude to my father.

Title: Turbulence in the solar wind from inertial to kinetic scales

Author: Alexander Pitňa

Department: Physics of Plasma and Ionized Media

Supervisor: Prof. RNDr. Jana Šafránková, DrSc., Physics of Plasma and Ionized Media

Abstract:

Solar wind, a stream of supersonic plasma emanating from the solar corona, serves as an ideal laboratory for a study of high Reynolds number plasma flows. Turbulent processes that govern the dynamics of the so-called inertial range, i.e., the spatial scales smaller than energy injection scales but larger than the scales where the dissipation processes set in, have been studied for decades. At present, it is believed that the large-scale free energy in a form of kinetic and magnetic fluctuations is transferred via turbulent cascade into smaller scales, where kinetic effects become dominant and heating takes place. In order to understand dissipation processes, high-cadence measurements of solar wind parameters are necessary. The bright monitor of the solar wind (BMSW) instrument on board the Spektr-R spacecraft provides such data, and in tandem with high-cadence measurements of the magnetic field from the Wind spacecraft, we are able address the nature of the sub-ion scale fluctuations. The thesis focus on three interconnected topics, (a) what changes are induced by the passage of a collisionless IP shock in the framework of turbulence, (b) study of a decay of the turbulent energy downstream an IP shock, and (c) identifying the dominant mode of the sub-ion scale fluctuations.

Keywords: turbulence, solar wind, kinetic range, inertial range

Název práce: Turbulence ve slunečním větru: od inerciální ke kinetické oblasti

Autor: Alexander Pitňa

Katedra: Katedra fyziky povrchu a plazmatu

Vedoucí disertační práce: Prof. RNDr. Jana Šafránková, DrSc., Katedra fyziky povrchu a plazmatu

Abstrakt:

Sluneční vítr, proud supersonické plazmy ze sluneční korony, je ideálním prostředím ke studiu toku plazmatu s vysokými hodnotami Reynoldsova čísla. Turbulentní procesy, které řídí dynamiku tzv. inerciální oblasti turbulence–tj. na škálách menších než charakteristické rozměry největších turbulentních víru, ale větších než charakteristické disipační škály–byly studovány po celá desetiletí. V současnosti se předpokládá, že volná energie obsažena ve fluktuacích na největších škálách ve formě magnetické a kinetické energie se přenáší prostřednictvím turbulentní kaskády do fluktuací na malých škálách, kde začnou dominovat kinetické efekty vedoucí k zahřátí plazmatu. Abychom pochopili procesy zpusobující disipaci na malých škálách, je nutno měřit parametry plazmatu s vysokou kadencí. Přístroj Bright monitor of the solar wind (BMSW) na družici Spektr-R je schopen měřit s časovým rozlišením 30 Hz a společně s rychlými měřeními magnetického pole družicí Wind, mužeme analyzovat fluktuace na charakteristických iontových škálách. Práce se zaměřuje na tři vzájemně provázaná témata spojená s turbulencí, (a) jaké změny vyvolává pruchod meziplanetárních rázových vln na charakter fluktuací, (b) studium rozpadu energie v oblasti za rázovou vlnou a (c) identifikaci dominantního plazmatického módu fluktuací na iontových škálách.

Klíčová slova: turbulence, sluneční vítr, kinetická oblast, inerciální oblast

"Look again at that dot. That's here. That's home. That's us. On it everyone you love, everyone you know, everyone you ever heard of, every human being who ever was, lived out their lives. The aggregate of our joy and suffering, thousands of confident religions, ideologies, and economic doctrines, every hunter and forager, every hero and coward, every creator and destroyer of civilization, every king and peasant, every young couple in love, every mother and father, hopeful child, inventor and explorer, every teacher of morals, every corrupt politician, every "superstar", every "supreme leader", every saint and sinner in the history of our species lived there-on a mote of dust suspended in a sunbeam."

Carl Sagan, Pale Blue Dot

Contents

Preface

Plasma, the so-called fourth state of matter, fills up the observable universe. During the photon epoch in the early cosmos, the plasma was literally ubiquitous. Roughly three hundred thousand years after the big bang at the epoch of recombination neutrals were formed for the first time and they filled the universe, entering the dark age era. When the first stars and galaxies were formed, the universe entered the reionization epoch and plasma started to play an ever more important role in the evolution of the observable matter.

A regime of motion that is inherent to the plasma fluid is a turbulent flow. At its simplest, if we understood a fluid flow through a pipe then we would know everything about turbulence—at least for the neutral fluid. The turbulent motion of a plasma is intricate due to a presence of the magnetic field and its fluctuations. Therefore, turbulence of a conducting fluid is especially difficult to describe.

Nevertheless, physics has been studying turbulence for over centuries and few of its fundamental properties are understood. The most important feature of turbulence is the existence of the so-called inertial range. It is a range of scales in which the fluctuations are self-similar and they do not depend on the initial stirring mechanism or the nature of dissipation, thus they follow the concept of universality. Although each realization of a turbulent system is unrepeatable and is random in space and time, statistical properties of fluctuations are not random. For this reason, any meaningful description of turbulent processes would be based on statistical averages.

It is believed that all important properties of hydrodynamic turbulence are contained in Navier-Stokes equations for the fluid motion (Falkovich and Sreenivasan, 2006); and for the plasma fluid in its magnetohydrodynamic (MHD) counterpart. Nowadays, many aspects of turbulence are studied via various computer simulations. The importance of these simulations is growing, ultimately thanks to Moore's law. However, observations power the engine of progress in understanding any physical phenomenon. Fortunately, an ideal laboratory for studying plasma turbulence is only a few tens of thousands kilometers away, outside the Earth's magnetosphere. Since the beginning of space explorations, dozens of satellites were dedicated to study the near Earth environment, the solar wind and Sun. The measurements from these spacecraft greatly enhanced our understanding of plasma turbulence.

In situ measurements of the solar wind plasma, which is a stream of protons, alpha particles, electrons and insignificant amount of heavier ions embedded in a magnetic field, allow us to study the onset of turbulence, its inertial range and the dissipation mechanism that ultimately transforms the free energy into an unorganized motion of particles. It is generally accepted that the apparent non-adiabatic radial temperature profile of the solar wind could be explained

by turbulent heating. Moreover, it is believed that turbulence could play a key role in the origin and the heating of the corona. The spacecraft that could help significantly in a search for a solution of these problems are either already in operation (Wind, Hinode, Magnetospheric Multiscale Mission, Parker Solar Probe) or in development (Solar Orbiter).

The topic of plasma turbulence is a wide area of research from both theoretical and observational points of view. This thesis focusses on *in situ* observations of solar wind turbulence. The thesis is organized as it follows. After the preface, chapter 1 reviews the origin and characteristics of the solar wind, including a brief summary of the most important microphysical processes. In chapter 2, the basic properties of turbulence are outlined—with respect to the regime that is relevant in the solar wind. Chapter 3 introduces the aims of the thesis. The analysis techniques are listed in chapter 4; the description of the spacecraft and relevant instruments onboard them whose data were analyzed are given in chapter 5. In chapter 6, the main results of the thesis are presented and the final remarks are summarized in chapter 7. The thesis is based on the papers published in the peer reviewed journals that are listed in the Attachments.

Chapter 1

Introduction

It was realized long before any *in situ* measurements that the space in between the Sun and the Earth is not empty and it is filled with some kind of particles. In 1859, a huge eruption on the surface of the Sun was observed by Carrington (1859) and Hodgson (1859), independently of each other. Only 17.6 hours later, a huge plasma cloud now called Coronal Mass Ejection-CME, hit the Earth's magnetosphere and caused a failure of telegraph systems over the world and, moreover, auroras were seen at latitudes as low as 20°. Therefore, it was inferred that there exists a new solar-terrestrial connection apart from an ever illuminating solar rays. A next important realization that the interplanetary space is filled with particles was made by Biermann (1951), who correctly deduced that there is a steady stream of "solar corpuscular radiation" coming from the Sun, thus explaining the anti-sunward direction of the comet tail and its deviation. In 1958, Alfvén (1958) correctly postulated that the solar wind is magnetized and in the same year, Parker (1958) showed theoretically that particles could indeed escape the Sun's gravity and form the solar wind.

In this chapter, a brief introduction to the origin and propagation of the solar wind is given. A macroscopic description of the solar wind is presented and relevant microphysical processes are described.

1.1 Macroscopic description of the solar wind

In a description of any physical system, it is important to realize what are the characteristic scales. The most straightforward one is the dimension of the system itself, D. In the case of the inner heliosphere, $D \simeq 1$ AU. The smallest scale for the solar wind plasma is the Debye length λ_{D} defined as:

$$\lambda_{\mathrm{D}} = \sqrt{\frac{\epsilon_0 k_{\mathrm{B}} T}{n e^2}}, \tag{1.1}$$

where ϵ_0 is the permittivity of vacuum, k_{B} is the Boltzmann constant, T is the temperature, n is the number density and e is the elementary charge. It is the spatial scale over which microscopic electric fields are screened out. It must hold that $\lambda_{\mathrm{D}} \ll D$ and $\lambda_{\mathrm{D}}^3 n \gg 1$. Indeed, in the solar wind at 1 AU, $\lambda_{\mathrm{D}} \simeq 10$ m $\ll 1$ AU and given its average density 10^7 particles per square meter, second condition holds also.

The two scales that are of vital importance are the so-called proton thermal gyroradius ρ_{gp} and proton inertial length ρ_{ip} defined as follows:

$$\rho_{\mathrm{gp}} = \frac{v_{p\perp}}{\Omega_{\mathrm{cp}}} \tag{1.2}$$

and

$$\rho_{\mathrm{ip}} = \frac{c}{\omega_{\mathrm{pp}}}, \tag{1.3}$$

where

$$\Omega_{\mathrm{cp}} = \frac{e|\boldsymbol{B}|}{m_{\mathrm{p}}} \tag{1.4}$$

and

$$\omega_{\mathrm{pp}} = \sqrt{\frac{n_{\mathrm{p}} e^2}{m_{\mathrm{p}} \epsilon_0}}. \tag{1.5}$$

Ω_{cp} is the gyrofrequency of protons in a magnetic field with the strength $|\boldsymbol{B}|$, $v_{p\perp}$ is the average velocity perpendicular to the magnetic field, c is the speed of light, ω_{pp} is the plasma frequency and m_{p} is the proton mass. The macroscopic description (MHD) is no longer valid below these scales.

Another scale of interest is the mean free path between the particles λ_{mfp}. In a plasma, the collisions are mediated through Coulomb force, therefore the mean free path is a product of Coulomb collision time, τ_{C} and the average thermal speed of the particles, v_{T}. In typical solar wind conditions at 1 AU, $\lambda_{\mathrm{mfp}} = \tau_{\mathrm{C}} v_{\mathrm{T}} = (2 \cdot 10^6\ s) \times (3 \cdot 10^4\ \mathrm{m} \cdot s^{-1}) = 6 \cdot 10^{10}$ m, which is roughly 1 AU. In average, the solar wind at 1 AU is a collisionless or a weakly-collisional plasma.

All of the quantities defined by eqs. 1.2-1.5 could be easily adopted for any other particle species, namely alpha particles or electrons. Because the solar wind consists mainly from protons and electrons, their characteristic scales will be the most relevant ones.

One should realize that the complete description of the origin and the consequent propagation of the solar wind plasma is a very complex problem due to the fact that the plasma undergoes a substantial expansion and all of the quantities defined above are functions of time and radial distance[1]. Therefore, any detailed analysis covers only a small part of the whole system. Despite the inherent non-stationarity of the processes that occur at the solar surface, in the chromosphere, solar corona and at the greater distances from the Sun, one can look at the average physical properties of each of these layers.

The plasma that eventually reaches the Earth starts its journey at the surface of the Sun, which is defined as bottom (or top) of the photosphere. Its thickness is around 500 km. Here, convective turbulent motions below the surface form granules approximately 10^3 km in diameter. These ever emerging and disappearing convecting cells feed the atmosphere above them with the solar plasma. The temperature and number density of photosphere is roughly 6000 K and 10^{17} cm^{-3}, respectively. Above the photosphere, 2000 km thick chromosphere lies, where the plasma is heated up to 20000 K and its density decreases to 10^{10} cm^{-3}. Then the plasma passes through the so-called transition region, where the density and temperature change drastically over a short distance of $\sim$ 500 km. Transition

[1] As Ulysses measurements revealed, they are also functions of the heliospheric latitude.

region ends at the height of $\sim$ 3000 km, where the temperature of the plasma exceeds $\sim$ 500000 K and the solar corona is forming. The number density at the base of the corona is roughly 10^9 cm^{-3}. The highest temperatures in the corona, $\sim 2 - 5 \cdot 10^6$ K, are reached in a distance of $\sim 2\ R_\odot$ from the solar surface, $R_\odot$ being the radius of the Sun. There is no clear upper boundary of the corona and it extends up to many tens of astronomical units. However, the plasma flow above $\sim\ 10\ R_\odot$ is usually denoted as the solar wind.

The question arises, why is it that the temperature of the outer atmosphere is orders of magnitude higher than that of the photosphere? This tantalizing question has not been answered yet. A source of energy for this heating are the convecting cells. The question is, how is the mechanical energy transformed into the magnetic energy and thermal energy. There are two sets of models that try to answer that. The first are the wave/turbulence-driven models (e.g. Jess et al., 2009) and the second are the reconnection/loop-opening models (e.g. Fisk et al., 1999). In the former models, it is assumed that the jostling of magnetic flux tubes launches Alfvén like fluctuations that propagate away from the surface where they are partially reflected and a strong MHD turbulence cascades the free energy down to the kinetic scales where it is dissipated. In the later models, it is assumed that millions of small-scale magnetic reconnection events take place between the open and closed flux tubes, each of them having energy equivalent to 10 Megaton nuke. Both models explain many observed features of the corona and solar wind. It is likely that both mechanisms are at work simultaneously, heating the corona together.

In the pioneering work of Parker (1958), the first theoretical description of the expanding solar atmosphere was given. The model qualitatively predicted the correct solar wind speed, given the temperature of the atmosphere is in the order of millions of Kelvins. Although it is very instructive, the model cannot account for the whole acceleration of the solar wind from many different reasons. An isothermal atmosphere is assumed, the pressure is isotropic, electromagnetic effects are not included, etc. It is clear from up-to-date observations that these assumptions are not fully justified. The solar wind is not isothermal, the temperature decreases with the radial distance. Observations showed that the decrease is not adiabatic and there is an excess of thermal energy within the solar wind plasma. This problem of "heating the solar wind" is yet an unresolved problem in the physics of the heliosphere. A detailed description of this problem and its connection to the MHD turbulence is given in Chapter 2. Finally, perhaps the most dubious simplification of the model is the neglection of the magnetic field and not accounting for a fact that the solar atmosphere is a plasma.

At the time when it was first realized that the Sun possesses a magnetic field, its origin was not clear. The primordial magnetic field that was likely present at the period of solar system formation but that would disappear rather quickly. After 4.5 billions of years none should be present. Therefore, many models of a solar dynamo have been developed, namely the "Parker Solar Dynamo Theory" (Parker, 1955) or "Babcock-Leighton model" (Babcock, 1961), each of them having its shortcomings (Piddington, 1972). Presently, two basic mechanisms that are responsible for a generation of the solar magnetic field are commonly used. The large scale magnetic structures, such as sunspots, are generated via "Global dynamo" (Nelson et al., 2014), placing the source of the magnetic field around

tachiocline, a thin layer between the radiative and convective zone with a strong velocity shear. On the other hand, the so-called "magnetic carpet" (Title and Schrijver, 1998), a highly structured mesh of magnetic north and south poles connected by magnetic field lines, seems to be generated by local flows of the plasma in the convecting cells, termed as the "local dynamo" process (Danilovic et al., 2010).

Once the magnetic field is present in the plasma, it is frozen into it. It is a natural consequence of plasmas' high conductivity and large dimensions of the system. Therefore, the plasma that escapes the solar surface carries magnetic field lines through all layers of the atmosphere. In the photosphere, the strength of the magnetic field varies from $\sim 10^{-4}$ T in the coronal holes up to ~ 0.3 T in the sunspots. At 1 AU, the average magnetic field strength is around $\sim 5 \cdot 10^{-9}$ T [2]. Close to the Sun ($R \lesssim 3\ R_\odot$), the magnetic field has a very complicated topology due to the presence of transient phenomena as CMEs, coronal loops, streamers, etc. However, roughly above 10 $R_\odot$ up to many astronomical units, a global topology of the magnetic field is archimedean spiral (see Fig. 1.1). This shape is a consequence of the constantly expanding plasma and frozen magnetic field lines. In the ecliptic plane, an angle between the radial velocity and magnetic field line, ψ gives the following formula:

$$\tan\psi = \frac{\Omega_\odot (R - R_\odot)}{V_{\rm sw}}, \tag{1.6}$$

where $\Omega_\odot$ is the angular speed of the Sun's rotation and it is $\psi \approx 45°$ at the Earth's orbit. The total magnetic field intensity, $|\boldsymbol{B}|$, decreases with the distance from the Sun, R, as follows:

$$|\boldsymbol{B}| = B_R(R_c) \left(\frac{R_c}{R}\right)^2 \sqrt{1 + \left(\frac{\Omega_\odot}{V_{\rm sw}}\right)^2 (R - R_c)^2}, \tag{1.7}$$

where $B_R(R_c)$ could be the solar dipole field at distance [3] R_c. Notice that close to the Sun, $R \geq R_c$, $|\boldsymbol{B}| \propto 1/R^2$ and at larger distances, $R \gg R_c$, $|\boldsymbol{B}| \propto 1/R$.

The role of the magnetic field in plasma processes captures a dimensionless parameter *plasma beta*, β defined as the ratio of the thermal pressure, P and magnetic pressure,

$$\beta = \frac{2\mu_0 P}{|\boldsymbol{B}|^2}, \tag{1.8}$$

where μ_0 is the permeability of the vacuum. It is important to realize that the pressure in magnetized plasma is a tensor and it may differ in directions parallel and perpendicular to the mean magnetic field. Therefore, kinetic instabilities that are connected with the pressure anisotropy play an important role in the microphysics of the solar wind. These kinetic processes will be described in the next section. However, in an ordinary MHD description of the large-scale solar wind plasma, the pressure is assumed to be a scalar.

The set of MHD equations that describes the plasma as a single magnetized

[2] If the Sun had a truly dipolar field and expanded into the vacuum, then the strength of the magnetic field would be 100 times lower at 1 AU.

[3] For a complete derivation of the formula see, e.g., Parks (1991).

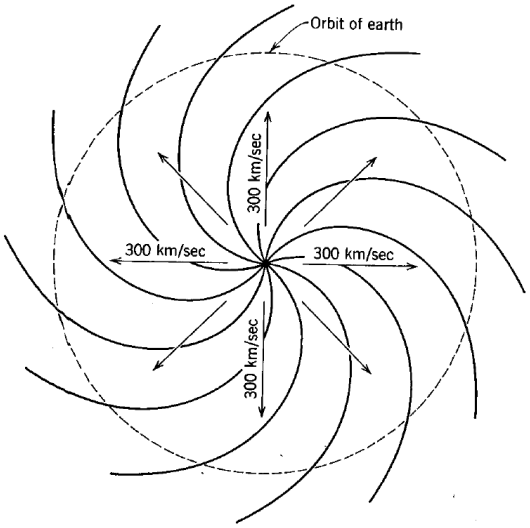

Figure 1.1: Adopted from Parker (1963).

fluid is listed in many textbooks on magnetohydrodynamics, e.g., Chen (1974); Priest (2014), therefore a full set is not shown here. However, it is instructive to show the continuity equation,

$$\frac{\mathrm{d}\rho}{\mathrm{d}t} + \rho \boldsymbol{\nabla} \cdot \boldsymbol{v} = 0, \tag{1.9}$$

and the equation of state,

$$\frac{p}{\rho^{\gamma}} = constant, \tag{1.10}$$

where γ is the polytropic index. It is easy to show that the density decreases as R^{-2}, assuming constant both solar wind speed and mass loss in eq. 1.9. Furthermore, taking the constant mass loss only, the implication is $\rho V_{\mathrm{sw}} = constant$ and this relationship is observed *in situ* (Withbroe, 1989). The equation 1.10—also known as the adiabatic law—tells that the plasma is essentially adiabatic, so there is no loss or gain of the internal energy. One can easily show that the temperature of the solar wind would behave as: $T \propto p/\rho \propto \rho^{2/3} \propto R^{-4/3}$, assuming $\gamma = 5/3$ in eq.1.10. Measurements show that the temperature profile is less steep, $T \propto R^{-\alpha}$, $\alpha = [0.5, 0.7]$ (Gazis et al., 1994; Richardson et al., 1995). This implies that as the solar wind expands, it is heated by some unknown mechanism. Where the excess of heat is coming from and what are the processes that dissipate the free energy, is the so-called "solar wind heating problem".

1.2 Kinetic aspects

Macroscopic and magnetohydrodynamic description of the plasma under stable conditions and transient phenomena in the corona and solar wind give a global picture of what is going on in the inner heliosphere. However, previous section introduced some of the key problems that the rather simple one-fluid MHD cannot explain. Namely, the dissipation of the free energy which is the ultimate process that heats the protons, electron and other ions. The processes that could con-

tribute to the overall heating of the plasma are kinetic in nature. In this section, a brief description of some of them is presented.

Due to the weakly collisional nature of the solar wind plasma, at first glance it seems reasonable to say that any non-thermal features of the distribution function of the particles will survive roughly one mean free path $\lambda_{\rm mfp}$. However, this is only partially true. In a plasma, there exists a variety of instabilities (see, e.g., Gary (1993); Marsch (2006)) and wave particle interactions that modify the velocity distribution function (VDF) in various ways, introducing a finite dissipation. Generally speaking, the VDF always "want" to be a Maxwellian and any significant deviation from this distribution gives rise to instabilities. In following paragraphs, the most relevant microphysical processes that occur in the solar wind are briefly mentioned.

In 1946, Landau discovered a collisionless mechanism that would dump an electromagnetic wave in an unmagnetized plasma; this process is named after him, *Landau damping*. For a detailed description of the mechanism see any good textbook on MHD. Shortly, an electromagnetic wave with phase velocity, $v_{\rm ph}$ will interact with particles whose speeds are $\sim v_{\rm ph}$. Since the Maxwellian VDF ($\propto e^{-v^2}$) has negative slope for $v > 0$, there are more particles gaining the energy from the wave than those that lose it to the wave, thus the wave is continuously damped. Here, it is important to mention that various wave modes and even waves with different wave-vectors of the same mode could have different damping rates, i.e., a shear Alfvén wave is weakly damped while a slow magnetosonic mode is heavily damped.

In a magnetized plasma, so-called resonant cyclotron wave-particle interactions frequently take place (see, e.g., Tsurutani and Lakhina (1997)). A condition when the exchange of energy between the wave—with frequency ω and wave-vector $\boldsymbol{k}$—and the particle with speed $\boldsymbol{V}$ occurs can be written as

$$\omega - \boldsymbol{k} \cdot \boldsymbol{V} = n\Omega_{\rm c}, \tag{1.11}$$

where n is an integer equal to $0, \pm 1, \pm 2, \cdots$ and $\Omega_{\rm c}$ is the cyclotron frequency. The equation can be understood as it follows: when a doppler shifted frequency of the wave is an integer multiple of the local cyclotron frequency, then the particle and wave are in phase and they can exchange energy and momentum. Note that if $n = 0$, the condition reduces to that of the Landau damping; the wave itself is damped independently of the presence of the magnetic field.

Next class of processes that could take place in the solar wind are driven by the pressure anisotropy $T_{\perp p}/T_{\parallel p}$, where $T_{\perp p}$ and $T_{\parallel p}$ are the proton temperatures perpendicular and parallel to the mean magnetic field, respectively; namely they are proton cyclotron, mirror, parallel and oblique fire hose instabilities and predicted by the Vlasov linear theory for Maxwellian electrons and bi-Maxwellian protons (Hellinger et al., 2006).

There are two main drivers of solar wind pressure anisotropy, its radial expansion and cyclotron resonance. The former causes a decrease of the perpendicular temperature $T_{\perp p} \propto R^{-2}$ while parallel temperature stays the same, $T_{\parallel p} = \text{const}$, thus decreasing $T_{\perp p}/T_{\parallel p}$. This behaviour is a consequence of the so-called double adiabatic (or CGL) system of MHD equations (Chew et al., 1956). The later increases the perpendicular temperature, thus increasing $T_{\perp p}/T_{\parallel p}$. The solar wind

plasma exhibits both regimes of anisotropy (see Fig. 1.2). In this Figure, the temperature anisotropy is plotted as a function of the parallel proton plasma beta, $\beta_{\parallel p}$. The right panel in Figure shows that the highly nonuniform distribution seems to be well constrained by the thresholds of oblique fire hose instability (for $\beta_{\parallel p} < 1$ and $T_{\perp p}/T_{\parallel p} < 1$) and mirror instability (for $\beta_{\parallel p} < 1$ and $T_{\perp p}/T_{\parallel p} > 1$).

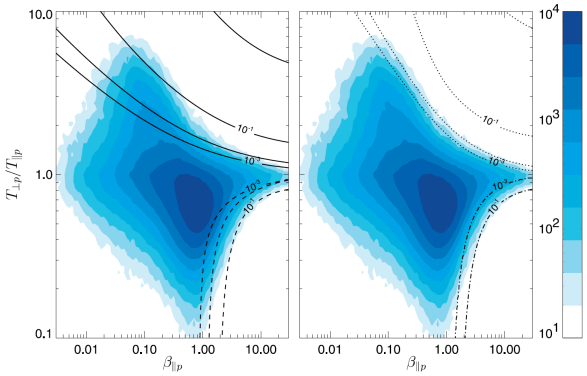

Figure 1.2: Relative frequency of $(\beta_{\parallel p}, T_{\perp p}/T_{\parallel p})$ at 1 AU for the Solar Wind Experiment (SWE) instrument on board the Wind spacecraft. Adapted from Hellinger et al. (2006).

Chapter 2

Linear and nonlinear phenomena in the solar wind

In the following chapter, a more detailed description of turbulent processes will be presented. First, we briefly introduce a linear Vlasov theory, focusing on the description of relevant plasma instabilities that occur in the solar wind. Second, we discuss a process of parametric instability which is a purely nonlinear phenomenon that is believed to occur in the solar wind and is connected with turbulence. Finally, a theoretical turbulent framework is introduced including characteristic time and spatial scales and decay laws.

2.1 Wave modes in plasma

In treatment of any astrophysical system under interest, it is vital to know the normal modes of this system. In other words, we need to understand what happens to the system if a small perturbation is introduced, what is its propagation properties, whether it is damped or it grows, etc. A linear theory can provide this information, however, it cannot describe the fate of the instability and it also cannot address any nonlinear couplings that are otherwise likely to be present in a real system. Nevertheless, if the amplitude of fluctuations is small, a linear theory is successful in describing them.

In order to determine the normal modes of system—in our case it is the solar wind plasma—there are more ways of achieving this goal. The simplest way is to perform a linear perturbation analysis of the MHD equations. However, any particular solution we find is limited by approximations used in the derivation of the MHD equations, i.e., wavelengths and frequencies cannot be arbitrary. Furthermore, any kinetic effects that can give rise to an instability are not present, thus the MHD approximation cannot capture all normal modes that the system can exhibit, naturally. However, in the limit of long wavelengths, MHD provides a good description of the normal modes in the most cases. In order to know what modes are present at the scales where MHD is no longer valid, i.e., at ion kinetic scales, one has to use more general equations.

Perhaps, the most suitable set of equations that account for the amount of

macro and micro-instabilities are Maxwell equations and the Vlasov equation:

$$\frac{\partial f_j}{\partial t} + \boldsymbol{v} \cdot \frac{\partial f_j}{\partial \boldsymbol{x}} + \frac{e_j}{m_j} \left(\boldsymbol{E} + \boldsymbol{v} \times \boldsymbol{B} \right) \cdot \frac{\partial f_j}{\partial \boldsymbol{v}} = \left(\frac{\partial f_j}{\partial t} \right)_{col}, \tag{2.1}$$

where $f_j = f_j(\boldsymbol{x}, \boldsymbol{v}, t)$ is the distribution function, e_j is the charge, m_j is the mass of the particle, where j denotes the particle species; E denotes the electric field. The unspecified collision term on the right hand side is assumed to be small and is set to zero, a valid assumption for a weakly-collisional solar wind.

In order to find the modes of the system, one should follow a well-established procedure (e.g., Gary (1993)). First, we assume that the amplitude of fluctuations is small, $F = F_0 + F_1$, where F is either the distribution function of particles, fluctuating magnetic or electric fields, or any other fluctuating physical quantity, whereas F_0 is not a function of time. Then, the fluctuating part is assumed in a form:

$$F_1 = F_1(\boldsymbol{x}, t) = F_1(\boldsymbol{k}, \omega) e^{i(\boldsymbol{k} \cdot \boldsymbol{x} - \omega t)}, \tag{2.2}$$

where $\boldsymbol{k}$ denotes the wave-vector and ω denotes the frequency. We define $k_\perp$ and $k_\parallel$ as the components of $\boldsymbol{k}$ perpendicular and parallel to the mean magnetic field, respectively. These components of $\boldsymbol{k}$ are real whereas ω is complex: $\omega = \omega_\mathrm{r} + i\gamma$. Then, the Vlasov equation is linearized and Fourier and Laplace transforms are applied on spatial and time coordinates, respectively. Finally, using the Maxwell equations, we obtain the dispersion equation that relates ω and $\boldsymbol{k}$. Solving for an explicit relationship $k = k(\omega)$ is unfeasible and the solution should be find numerically in the most cases.

It is beyond the scope of the thesis to list all possible modes that the plasma can support and only the most relevant for the solar wind will be described. For convenience, the fluctuations can be divided into two categories depending on their wave-vector: (a) macroscopic for $k\rho_\mathrm{gp} < 1$ and (b) microscopic for $k\rho_\mathrm{gp} \gtrsim 1$. In the discussion of wave modes relevant for inertial range turbulence, i.e., the case (a), the fluid equations give similar results[1] as the above mentioned procedure. However, at the high wave-number end of the inertial range of turbulence, MHD is no longer valid and the Vlasov-Maxwell theory predicts a number of modes that are observed in the solar wind. At scales $k\rho_\mathrm{gp} \gtrsim 1$, most of the dissipation of free energy occurs and therefore it is vital to understand the nature of the fluctuation in this range.

2.1.1 Modes at $k\rho_\mathrm{gp} < 1$

In this regime, the MHD theory gives well understood modes; namely: intermediate (shear or Alfvén), fast and slow modes. Observations show that the Alfvén mode is the most dominant in the solar wind and comprises around $\sim 90\%$ of the energy within the fluctuations, whereas the slow mode only $\sim 10\%$ (Klein et al., 2012). For the most important Alfvén mode, MHD solution gives zero fluctuations along the magnetic field line, $\delta B_\parallel = 0$, therefore it is incompressible. On the other hand, the fast and slow MHD magnetosonic modes are compressive $|\delta B_\parallel| > 0$, and density fluctuations are either positively or negatively correlated

[1] However, in certain parameter regime $\{\theta, \beta, T_\mathrm{e}/T_\mathrm{p}\}$, the Vlasov theory gives different damping rates of some modes. For details, see Gary (1993).

Phase speeds	weakly damped regime	identification
	$\beta_{\rm p} \ll 1$	
Slow	$Q_\parallel$ if $T_{\rm e} \gg T_{\rm p}$	Ion acoustic
Intermediate	All θ	Alfvén
Fast	$Q_\parallel$	Parallel magnetosonic
Fast	$Q_\perp$	Magnetosonic
	$\beta_{\rm p} > 1$	
Slow	All θ	Alfvén
Intermediate	$Q_\parallel$	Parallel magnetosonic
Fast	$Q_\parallel$ if $T_{\rm e} \gg T_{\rm p}$	Ion acoustic
Fast	$Q_\perp$	Magnetosonic

Table 2.1: Nomenclature of low frequency waves. $Q_\parallel$ and $Q_\perp$ denote the "quasi-parallel" and "quasi-perpendicular" regime and θ denotes the angle between the mean magnetic field vector and wave vector. Adopted from Gary (1993).

with $\delta B_\parallel$ fluctuations for both modes, respectively. Dispersion relation for the Alfvén mode is trivial and it reads

$$\omega = k_\parallel v_{\rm A}, \tag{2.3}$$

where $v_{\rm A}$ is the Alfvén speed. The dispersion relation of the other two modes are more complicated and we only note that the phase speed of the modes is well separated for all propagation angles except purely perpendicular or parallel $\boldsymbol{k}$.

What the linear MHD analysis cannot account for are the damping rates of these modes and the Vlasov-Maxwell description is more appropriate even for the long-wavelength waves for the collisionless solar wind. The Vlasov-Maxwell solution of intermediate Alfvén mode gives a non-vanishing $\delta B_\parallel$ which is $k_\perp$ dependent (TenBarge et al., 2012). Furthermore, one mode can have different damping rates for high or low β, quasi-parallel or quasi-perpendicular propagations, or for different values of electron/temperature anisotropy. For clarity, the nomenclature of the Vlasov-Maxwell low-frequency weakly-damped wave modes is given in Table 2.1.

2.1.2 Modes at $k\rho_{\rm gp} \gtrsim 1$

At kinetic scales, the electromagnetic modes of Vlasov-Maxwell equations that are the most relevant for the solar wind are the whistler mode and the so-called kinetic-Alfvén (KAW) mode. Many authors described these modes (e.g., Gary (1993); Hollweg (1999); Howes et al. (2006); Schekochihin et al. (2009)), however, Boldyrev et al. (2013) provided probably the most comprehensive derivation of various physical characteristics of these modes together with approximate but explicit formulas in various regions of the $\omega - k_\perp$ space.

The dispersion relation of KAWs for nearly perpendicular wave-vectors $k_\perp \gg k_\parallel$ and for $k_\perp \rho_{\rm gp} \gg 1$ can be expressed as

$$\omega^2 = \frac{v_{\rm A}^2 \rho_{\rm s}^2 \left(1 + \frac{T_{\rm p}}{T_{\rm e}}\right)}{1 + \frac{v_{\rm s}^2}{v_{\rm A}^2}\left(1 + \frac{T_{\rm p}}{T_{\rm e}}\right)} k_\parallel k_\perp, \tag{2.4}$$

where we introduce an ion-acoustic scale $\rho_s = v_s/\Omega_{cp}$, $v_s = \sqrt{T_e/m_p}$ being the ion-acoustic speed and T_p and T_e being proton and electron temperatures (Schekochihin et al., 2009; Boldyrev et al., 2013).

The dispersion relation for the whistlers, assuming low obliqueness $k_\parallel \rho_{gp} \gg 1$ and the frequency to lie within $kv_p \ll \omega \ll k_\parallel v_e$, has a form

$$\omega^2 = \frac{v_A^4 \rho_s^2}{v_s^2} k_\parallel^2 k^2. \tag{2.5}$$

The key difference between these two modes is a role of protons in the dynamics of their fluctuations. KAWs are compressible modes due to their low frequency $\omega \ll k_\perp v_p$. Compressibility of the KAW waves, C_{KAW} can be expressed as

$$C_{KAW} \equiv \frac{(\delta n_e/n_0)^2}{(\delta B/B_0)^2} = \frac{1}{2\frac{v_p^4}{v_A^4}\left(1+\frac{T_i}{T_e}\right)^2 + \frac{v_p^2}{v_A^2}\left(1+\frac{T_i}{T_e}\right)}, \tag{2.6}$$

where δn_e denotes electron density perturbation around some background value n_0, δB denotes the magnetic field perturbation and B_0 is the magnitude of a non-fluctuating background magnetic field.

It can be seen that while the compressibility does not depend on k, it strongly depends on plasma beta $\beta_p = v_p^2/v_A^2$. For an average solar wind plasma beta ≈ 0.3 and eletectron/proton temperature ratio ≈ 2 eq. 2.6 yields $C_{KAW} \approx 1$. Furthermore, KAWs exhibit an interesting behaviour (Zhao et al., 2014): for a parallel propagation, their polarization is left-handed and the electric field rotates in the same sense as protons, thus they can be damped; however, for a highly oblique propagation, the polarization reverses and thus they can exist above and below the ion-cyclotron frequency because the damping is not strong. On the other hand, whistlers are electron waves, thus the ions are not dynamically important and serve as a stationary background. Compressibility of the whistlers can be expressed as

$$C_w \equiv \frac{(\delta n_e/n_0)^2}{(\delta B/B_0)^2} = \frac{1}{2}\frac{\omega_{pp}^4}{k_\parallel^4 c^4} = \frac{1}{2}\frac{1}{(k_\parallel \rho_{ip})^4}. \tag{2.7}$$

For $\beta_p \approx 1$ and $k_\parallel \rho_{gp} > 1$ it yields $C_w \ll 1$. Note that if the inertial length and thermal gyroradius are equal then proton plasma beta is unity.

2.2 Parametric instability

In the previous two sections, a brief description of linear modes was given. Considering the long wave-length modes, one can ask: how stable are these solutions? In general, when parameters of a physical system are periodically varied then the normal modes of the system can be excited. In the case of the Alfvén wave, the physical system is the solar wind plasma and the parameter that is being varied is the magnetic field of the Alfvén (or pump) wave. According to Hollweg (1994), parametric instabilities for Alfvén waves can be divided into three classes: (a) decay, (b) modulational, and (c) beat instability. Here, we will focus on the first class, i.e., Parametric Instability Decay (PID).

Early works of Sagdeev and Galeev (1969) and others showed that the forward

propagating Alfvén wave decays into forward propagating sound wave and backward propagating Alfvén wave. It was realized that PID could be responsible for the existence of the backward propagating Alfvén waves in the solar wind, which are necessary for MHD turbulence to develop (see chapter 2.3). Therefore, many theoretical and simulation studies addressed the importance of PID for the solar wind plasma.

Sagdeev and Galeev (1969) studied PID of a linearly polarized Alfvén wave in the limit of small plasma beta $\beta \ll 1$ and small amplitude of the pump wave $\delta B/B_0 \ll 1$. They estimated the growth rate of PID as

$$\frac{\gamma}{\omega_0} \approx \frac{1}{2}\frac{\delta B}{B_0}\frac{1}{\beta^{1/4}}, \tag{2.8}$$

where ω_0 is the frequency of the pump wave. A more appropriate case of circularly polarized Alfvén wave for finite $\delta B/B_0$ and β was studied by Derby (1978) and Goldstein (1978). They showed that for low plasma beta, PID has significant growth rates even for small amplitudes of the pump wave $\delta B/B_0 \approx 0.01$.

When numerical simulations of MHD turbulence become feasible, the growth rates and a saturation of PID in quiet and turbulent plasmas were investigated. PID for oblique and parallel propagations was studied by Del Zanna (2001) and Matteini et al. (2010). The effects of solar wind expansion on PID were investigated by Tenerani and Velli (2013) and Del Zanna et al. (2015). More recently, Shi et al. (2017) investigated PID in the turbulent environment via simulations of ideal MHD. They found that the growth rates of PID (compared to linear predictions) were reduced by $\approx 50\%$. Fu et al. (2018) employed a hybrid simulation (kinetic ions and fluid electrons) and showed that the growth rates are also reduced, and moreover, they observed Landau damping of the ion acoustic waves generated by PID, thus showing that it can provide an important channel for energy dissipation of the inertial-range Alfvén waves.

A direct observation of PID within the Earth's foreshock was reported by Spangler et al. (1997). They concluded that while the instability can be excited, it cannot fully develop due to insufficient lifetime of the pump wave and therefore it would not play a significant role in the foreshock dynamics. On the other hand, it is believed that PID can play a key role in the solar coronal heating in a very low-beta environment near the transition region of the solar atmosphere (Gary, 2001; Pruneti and Velli, 1997). Furhermore, Del Zanna et al. (2015) speculated that PID can explain the break in the fluctuation power spectra between the injection and inertial ranges and the onset of turbulence below L_i (see Fig. 2.1).

Despite the growing number of studies showing that PID could play a significant role in the dynamics of the turbulent solar wind, it is not known how big its contribution really is.

2.3 Turbulence in the solar wind

In this section, some key aspects of MHD turbulence and its early solar wind observations will be outlined. It should be stressed that despite the decades of theoretical and observational advances, a satisfactory picture of what is really happening in open astrophysical system is still missing. This state follows from

the difficulty of solving the Navier-Stokes equations for a conducting fluid. Even their simplified version for incompressible fluid is not fully understood. When assuming the mass density to be spatially uniform, incompressibility and fluid velocity to be significantly lower than the slowest speed of compressible wave propagation, then the set of incompressible MHD equations is

$$\frac{\partial \boldsymbol{u}}{\partial t} + \boldsymbol{u} \cdot \boldsymbol{\nabla} u = -\boldsymbol{\nabla} p + \nu \Delta \boldsymbol{u} + \boldsymbol{B} \cdot \boldsymbol{\nabla} \boldsymbol{B} + f, \tag{2.9}$$

$$\frac{\partial \boldsymbol{B}}{\partial t} + \boldsymbol{u} \cdot \boldsymbol{\nabla} B = \boldsymbol{B} \cdot \boldsymbol{\nabla} \boldsymbol{u} + \eta \Delta \boldsymbol{B}, \tag{2.10}$$

$$\boldsymbol{\nabla} \cdot \boldsymbol{v} = \boldsymbol{\nabla} \cdot \boldsymbol{B} = 0, \tag{2.11}$$

where $\boldsymbol{u}$ is the velocity field, p the pressure scaled by constant density ρ_0, $\boldsymbol{B}$ magnetic field scaled by $\sqrt{4\pi\rho_0}$, ν the kinematic viscosity, η the magnetic diffusivity, and f the external force.

Two important dimensionless parameters that characterize the state of the flow and that can be easily obtained from the equations above are the kinetic Reynolds number, Re and magnetic Reynolds number, $Re_{\rm m}$ defined as follows

$$Re = \frac{L_0 u_0}{\nu} \tag{2.12}$$

and

$$Re_{\rm m} = \frac{L_0 u_0}{\eta}, \tag{2.13}$$

where L_0 is the scale of the system, or the characteristic scale of the largest eddies within the turbulent flow.

Basically, Re is the ratio between the inertial and viscous forces and $Re_{\rm m}$ is a measure of the coupling between the flow and magnetic field, i.e., when $Re_{\rm m} \gg 1$ then the coupling is strong and we are in the so-called frozen-in approximation. In the case of $Re_{\rm m} \ll 1$, the coupling is weak and the magnetic field diffuses rather quickly.

In the case of the HD flow, observations show that turbulence occurs for $Re \gg 1$. This happens when the free energy supplied at large spatial scale $L_{\rm i}$ cannot be dissipated by the viscous forces at the time scale $\approx L_{\rm i}/\delta v$, where δv denotes the velocity fluctuations of the eddies at scale $L_{\rm i}$. In other words, the spatial scale at which viscosity becomes dominant l_ν is orders of magnitude smaller than $L_{\rm i}$. A relation between the injection scale $L_{\rm i}$, dissipation scale l_ν and Re is

$$Re \sim \left(\frac{L_{\rm i}}{l_\nu}\right)^{\frac{4}{3}}, \tag{2.14}$$

see, e.g., Davidson (2004). When $Re \gg 1$, the scales are clearly separated and they define the so-called *inertial range* within which turbulence operates.

Other dimensionless parameter that characterizes the nature of the flow is the magnetic Prandtl number. It is defined as the ratio between magnetic and kinetic Reynolds numbers

$$Pr_{\rm m} = \frac{Re_{\rm m}}{Re} = \frac{\nu}{\eta}. \tag{2.15}$$

On interstellar and galactic scales, this number tends to be very large; $Pr_{\mathrm{m}} \gtrapprox 10^{11}$ and $Pr_{\mathrm{m}} \gtrapprox 10^{29}$, respectively. On the other hand, within stellar convection zones, $Pm_{\mathrm{m}} \ll 1$. In the solar wind, the Prandtl number $\gtrapprox 1$. The importance of this number is that it relates the magnetic diffusion scale l_η and viscous dissipation scale l_ν as

$$l_\eta \sim {Pr_{\mathrm{m}}}^{-1/2} l_\nu, \tag{2.16}$$

i.e., when $Pr_{\mathrm{m}} \gg 1$ then $l_\eta < l_\nu$ and spatially smooth random motions at the viscous scale contribute significantly to the stretching of the magnetic field which causes an increase of the magnetic field, thus maintaining the small-scale dynamo (Schekochihin et al., 2007). However, this process requires weak magnetic field in a sense that $\delta B \gg \boldsymbol{B}_0$. In the solar wind, $\delta B \lesssim \boldsymbol{B}_0$ is much more common.

The characteristic scales of turbulence defined above; namely L_{i}, l_{D}, l_ν and l_η can be estimated from the *in situ* measurements. When analyzing single-point measured data, a condition a conversion between temporal and spatial scales is a so-called Taylor hypothesis (Taylor, 1938). It simply states that the characteristic time of fluctuations is shorter than the time needed for the spacecraft to measure that fluctuation, i.e., the spacecraft sweeps through the plasma so fast that the fluctuations have little time to change. In the solar wind, this condition is expressed as $|\boldsymbol{v}_A| \ll |\boldsymbol{v}_{\mathrm{sw}}|$, where $\boldsymbol{v}_{\mathrm{sw}}$ denotes the solar wind speed, and it is usually well satisfied. Then, the fluctuations measured at the time scale t in the spacecraft frame can be viewed as spatial fluctuations at the scale $|\boldsymbol{v}_{\mathrm{sw}}|t$.

Figure 2.1 show the sketch of a Power Spectral Density (PSD) of a physical quantity that undergoes a turbulent cascade, i.e., ion velocity, density, magnetic field, etc. The power spectrum is a function of the power within the fluctuations as a function of scale l. The turbulent scales are depicted as vertical lines and show a relation with the characteristic breaks in the spectrum. The parts of the spectrum are usually well approximated by a power law function $PSD \propto l^{-a}$. On large scales, $l > L_{\mathrm{i}}$, the spectrum is a power law with $a \sim 1$, in the inertial range, the slope is steeper $a \sim \langle 1.5, 2 \rangle$, and finally, in the dissipation range, the spectrum has a slope $a \gtrsim 2$. The break at larger scales is connected with the injection scale, and can also be viewed as the scale of the largest eddies. Therefore, it can be identified as a coherence length L_{c}. At the viscous scale l_ν, the break in the spectrum is associated with two turbulent characteristic scales (a) Taylor microscale, l_{T} and (b) Kolmogorov microscale, l_{K}, the former can be viewed as the scale at which the viscosity begins to strongly affect the eddies while the later is defined as the smallest scale in the turbulent flow; therefore $l_{\mathrm{T}} > l_{\mathrm{K}}$. A relationship between the scales is $l_{\mathrm{K}} \sim l_{\mathrm{T}} Re^{-1/4}$ (Batchelor, 1982; Davidson, 2004).

The single-point measurements of solar wind plasma can be used to determine the above mentioned characteristic turbulent scales and the power laws in different ranges of scales. Thus, they can be used to infer in what turbulent framework matches the solar wind plasma and can show which dynamical processes dominate at various spatial scales. In HD turbulence, the injection or coherence scale is comparable to the dimensions of the obstacle, spacing of the grid in a wind tunnel, etc. However, in the solar wind there is no obvious length scale that could be associated with this scale. Considering the observations at 1 AU, the characteristic injection scale is in the order of millions of kilometers, $L_{\mathrm{i}} \sim 2 \cdot 10^6$ km (Jokipii and Hollweg, 1970; Matthaeus et al., 1986). This implies that

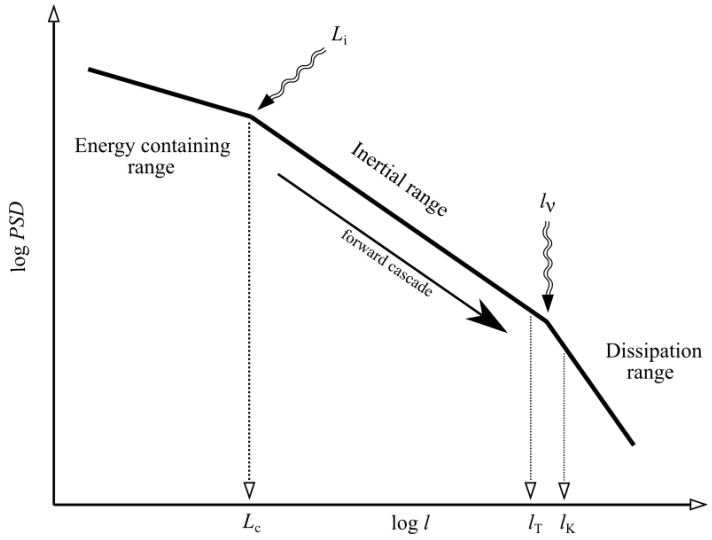

Figure 2.1: Sketch of the turbulent power spectrum and its characteristic scales.

the spatial fluctuations at larger scales are not a part of the turbulent cascade and they are the product of coronal dynamical processes. However, Bruno et al. (2009) showed that these fluctuations become a part of the cascade as the turbulence ages. On the opposite side of the inertial range, *in situ* measurements show that the characteristic dissipation scale is in the order of the characteristic ion scales, $\rho_{\mathrm{gp}} \simeq \rho_{\mathrm{ip}}$, i.e., in the order of hundreds of kilometers (Leamon et al., 1998; Chen et al., 2014a; Šafránková et al., 2013b). When we insert these scales into eq. 2.14, a rough estimate of the Reynolds number yields $Re \simeq 200000$.

Furthermore, multi-point spacecraft measurements provide an independent estimation of the Reynolds number. Matthaeus et al. (2005) computed the correlation scale and Taylor scale in the solar wind at 1 AU using simultaneous two point measurements of pairs of the spacecraft. A formula that quantitatively estimates the so-called effective magnetic Reynolds number (Batchelor, 1982; Matthaeus et al., 2005) is as follows

$$Re_{\mathrm{m}}^{\mathrm{eff}} = (\lambda_{\mathrm{c}}/\lambda_{\mathrm{T}})^2. \tag{2.17}$$

They estimated that $Re_{\mathrm{m}}^{\mathrm{eff}} \simeq 200000$.

These measurements show that the presence of turbulence within the solar wind is firmly established. In fact, this was first realized by Coleman (1968) who interpreted measurements from the Mariner 2 spacecraft as a manifestation of a turbulence cascade because the power of fluctuations over a wide range of scales decreases as a power law. As more satellites dedicated to study the solar wind were launched, such as Helios and Ulysses, together with the advancements in the theory of MHD turbulence, it started to be clear that turbulent processes play a significant role in the evolution of the solar wind plasma. In 1976, Helios I and II periodically crossed the same high-speed stream in various distances from the Sun, thus these spacecraft had been able to measure the radial dependence of a level of the turbulent fluctuations between 0.3 and 0.9 AU. Bavassano et al. (1982) analyzed whole four crossings and found that the power within the fluctuations decreases roughly as $R^{-3.5}$ which is faster than the prediction of geometric optics for the noninteracting large scale Alfvénic fluctuations in the

expanding solar wind, R^{-3}, i.e. WKB approximation (for more details see, e.g., Barnes (1979); Hollweg (1973)). Furthermore, Bruno et al. (2009) combined the Ulysses measurements at distances 1.4 and 4.8 AU with those of Helios (see Figure 2.2). In the figure, the power spectra of the magnetic field for slow and fast wind are presented. Fast wind spectra exhibit a clear break at low frequencies which separates the injection scale from the inertial range of turbulence. The frequency of this break, f_{B} shifts to a lower frequency with larger heliocentric distances as $f_{\mathrm{B}} \propto R^{1.52}$; indicating that nonlinear interactions are present during the expansion.

On the other hand, the slow solar wind does not exhibit the break in the power spectra, at least not at the frequencies comparable to those within the fast wind. Recently, Matteini et al. (2018) attributed the absence of this break to the condition $\delta B/B_0 \ll 1$. This condition reflects the fact that the slow wind has a lower level of fluctuations on average. Moreover, the fluctuations are less Alfvénic, i.e., the correlation between the magnetic and velocity fluctuations is close to zero, and they are more compressible, i.e., $\delta|B|/B_0 \gtrsim 0.1$ (Grappin et al., 1991). Nonetheless, the presence of turbulence within the slow wind is firmly established (Tu and Marsch, 1995; Horbury, 1999; Bruno and Carbone, 2013; Marsch, 2018).

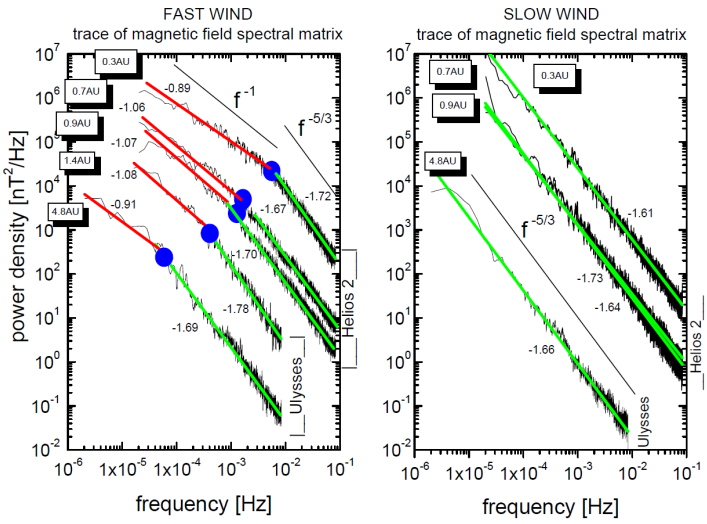

Figure 2.2: Power density spectra of magnetic field fluctuations observed by Helios 2 and Ulysses for fast (left panel) and slow (right panel) solar winds. Image adapted from Bruno et al. (2009).

In the following subsections, we focus on both the phenomenological description and observational evidence of the turbulent cascade. The former will provide us with the framework in which the later should be viewed. One could argue that phenomenological descriptions evolve in order to explain the ever growing number of new observations and, *vice versa*, newly developed description of some physical process could trigger an observational campaign. However, in the field of turbulence, the situation is biased towards the observations. This is a consequence of the above mentioned fact that although the Navier-Stokes equations for a plasma fluid are known for decades, we still do not know how the solutions look like. In order to get any laws that can be tested against the real data, a phenomenological

view has to be adopted.

Nevertheless, many features that are observed in the solar wind can be successfully explained by phenomenological theories. In order to introduce these theories, we start with a general description of the system. The spatial scales of the system were introduced in chapter 1.3 and include the injection scale $L_{\rm i}$ and dissipation scale l_ν. In sub-section 2.3.1, the characteristic time scales in the system will be introduced. Sub-section 2.3.2 will introduce the phenomenological description of Kolmogorov inertial range turbulence, from which the MHD counterparts originate, namely, the Iroshnikov-Kraichnan and Goldraich-Sridhar ideas. The kinetic range of solar wind turbulence will be described in sub-section 2.3.3. Finally, we will return to the large scale dynamics of turbulence in chapter 2.3.4, where the decay laws for various turbulent scenarios will be presented.

2.3.1 Characteristic time scales

Since we are focussed on solar wind turbulence, let us first define two time scales associated with the expansion: they are the transport time, $\tau_{\rm tr}$ and adiabatic time, $\tau_{\rm ad}$ defined as

$$\tau_{\rm tr} = \frac{R}{|\boldsymbol{V}_{\rm sw}|} \tag{2.18}$$

and

$$\tau_{\rm ad} \sim \frac{1}{\boldsymbol{\nabla}\cdot\boldsymbol{V}_{\rm sw}} = -\frac{1}{\rho_{\rm s}}\frac{{\rm D}\rho_{\rm s}}{{\rm Dt}}, \tag{2.19}$$

where $\rho_{\rm s}$ is the specific volume. The meaning of the transport time is straightforward. The adiabatic time describes the rate of change of the specific volume and is of the same order as the transport time.

The third time timescale is the so-called nonlinear eddy turnover time, $\tau_{\rm nl}$ defined as

$$\tau_{\rm nl} \sim \frac{l}{\delta v_l}, \tag{2.20}$$

where δv_l is the velocity fluctuation amplitude within a turbulent eddy of spatial scale l. The turbulence operates on this timescale, i.e., (a) when turbulence is generated, one expects several eddy turnover times in order to observe a fully developed turbulence, and (b) transfer of energy of large-scale fluctuations into smaller ones proceed roughly over this timescale. In the solar wind around 1 AU, the ordering of the timescales of the inertial range fluctuations is as follows: $\tau_{\rm nl} < \tau_{\rm tr} \sim \tau_{\rm ad}$. The inequalities show that there is enough time for observing fully developed turbulence and that it is not strongly affected by the expansion, at least in this rather simplified view.

Fundamental property of turbulence in any phenomenological description is a notion that the energy which is supplied at the injection scale $L_{\rm i}$ at rate $\Pi_{\rm i}$ is dissipated at kinetic scales l_ν with the dissipation rate ϵ and no energy is lost in the inertial range, where the nonlinear interactions respect the conservation of energy. Therefore, following equalities hold true:

$$\Pi_{\rm i} = \Pi(l) = \epsilon, \tag{2.21}$$

where $\Pi(l)$ denotes the energy transfer rate in the inertial range. Energy injection

rate can be estimated roughly as the ratio of the turbulent free energy at the injection scale $\sim (\delta v_l)^2$ and eddy turnover time $\tau_{\rm nl}$ yielding

$$\Pi_{\rm i} = \epsilon \sim \frac{(\delta v_l)^2}{\tau_{\rm nl}} = \frac{(\delta v_l)^3}{l}. \tag{2.22}$$

The equation leads to $\delta v_l \sim (\epsilon l)^{1/3}$ and when we insert this expression back into eq. 2.20 we get

$$\tau_{\rm nl}(l) \sim \epsilon^{-1/3} l^{2/3}. \tag{2.23}$$

It is now clear that the eddy turnover time depends on the spatial scale of interest. At the injection scale, the nonlinear time is the largest and the eddies contain most of the turbulent energy of the system. At the end of the inertial range, the turbulent time scale is much shorter and the cascade proceeds quickly, adjusting itself to the incoming flux of energy from the larger scales. Therefore, the largest eddies control the dynamics of the turbulent system.

2.3.2 Inertial range

Firstly, we will briefly review the so-called K41 phenomenological theory of turbulence of Kolmogorov (1941) because nearly all phenomenological models of MHD turbulence are based on it. The famous Kolmogorov "5/3" law reads

$$E(k) = C_{\rm K} \epsilon^{2/3} k^{-5/3}, \tag{2.24}$$

where $E(k)$ denotes the spectral energy density per unit mass and $C_{\rm K}$ is the dimensionless Kolmogorov constant. It can be derived by a dimensional analysis under some assumptions about the nature of turbulence: $E(k)$ can be expressed as

$$E(k) = \frac{\Delta E}{\Delta k} \tag{2.25}$$

and dimensionally

$$[E(k)] = \frac{[\Delta E]}{[\Delta k]} = \frac{m^2 \cdot s^{-2}}{m^{-1}} = m^3 \cdot s^{-2}, \tag{2.26}$$

where $\Delta k = k_1 - k_2$ is the wave-number interval carrying energy ΔE of fluctuations. Now, the key assumption—the so-called *second Kolmogorov hypothesis*—is that the spectral energy density depends solely on the energy injection rate ϵ and the spatial scale l. Therefore, one can write

$$[E(k)] = C_{\rm K} \epsilon^{\alpha} k^{\beta} \tag{2.27}$$

together with

$$[E(k)] = [\epsilon]^{\alpha} [k]^{\beta} = (m^2 \cdot s^{-3})^{\alpha} (m^{-1})^{\beta}. \tag{2.28}$$

By equating units of lengths and times in eqs. 2.26 and 2.28, we get a system of two linear equations whose solutions are the exponents in the eq. 2.24.

In the derivation, we used an approximation, $\Delta E \approx (\delta v_l)^2$. A more precise

expression of δv_l is

$$\delta v_l = \langle \delta \boldsymbol{v}(l) \rangle = \langle \boldsymbol{v}(\boldsymbol{x} + \boldsymbol{l}) - \boldsymbol{v}(\boldsymbol{x}) \rangle \,, \tag{2.29}$$

where angle brackets denote the spatial average. Note that we also assumed that l have to be small compared to the injection scale and larger than the Kolmogorov scale, $l_\mathrm{i} \gg l \gg l_\mathrm{K}$. In the absence of a preferential direction within the fluid flow, thus assuming isotropic turbulence, the mean velocity fluctuation depends only on the modulus of $\boldsymbol{l}$.

For hydrodynamic flows, the assumption of an isotropic turbulence is reasonable and the Kolmogorov "5/3" law is observed experimentally and in computer simulations. However, in MHD flows, the magnetic field introduces an anisotropy and additional time scale(s).

We begin the treatment of inertial range MHD turbulence in the framework of Zhou et al. (2004). Due to many possible regimes of MHD turbulence, i.e., importance of the magnetic field for the turbulence dynamics (isotropic vs. anisotropic), balanced vs. imbalanced fluxes of oppositely propagating fluxes of Alfvén waves, dominant processes of spectral energy transfer, etc., Zhou et al. (2004) attempted to unify the MHD turbulence framework by introducing the phenomenological steady energy transfer rate (see eq. 2.21) in a form

$$\epsilon = \Pi(k) = \tau_\mathrm{T}(k) \frac{kE(k)}{\tau_\mathrm{nl}^2}, \tag{2.30}$$

where τ_T is the triple correlation time and τ_nl is the nonlinear dynamical time scale. The triple correlation time is the time scale governing the decay of triple velocity correlations that induce the spectral energy transfer, whereas τ_nl is the time scale of the nonlinear interactions. Basically, different regimes of turbulence can be described by substituting particular expressions for these time scales.

First, let us introduce the concepts of the straining and sweeping processes in the context of MHD turbulence. In hydrodynamics, the interactions between the eddies of the same size consist of straining motions, i.e., gradients in velocity of the neighbour vortexes will distort these vortexes. This process is in its nature local and its characteristic time scale is given by eq. 2.20. On the other hand, the sweeping is a non local process of interactions of large and small scales. In MHD, this process is often termed as the Alfvén propagation effect, i.e., large-scale Afvénic fluctuations displace the small-scale structures. Characteristic time scale of the sweeping is given by the Alfvén crossing time of the given length scale l:

$$\tau_\mathrm{A} \sim \frac{l}{v_\mathrm{A}}, \tag{2.31}$$

where

$$v_\mathrm{A} = \frac{B_0}{\sqrt{\mu_0 \rho_0}} \tag{2.32}$$

is the Alfvén speed.

Interplay between the Alfvén and nonlinear time scales plays an essential role in distinguishing the various turbulence regimes. Zhou et al. (2004) derived scaling laws for many of the regimes. Here, only the most relevant scenarios for the solar wind will be outlined.

Iroshnikov-Kraichnan $-3/2$ scaling

Under the assumptions of (a) isotropic large-scale magnetic field and that (b) the energy transfer is dominated by the sweeping processes, then eq. 2.30 leads to well-known scaling derived by Iroshnikov (1963) and Kraichnan (1965) (IK65),

$$E(k) = (v_{\rm A}\epsilon)^{1/2} k^{-3/2}. \tag{2.33}$$

In the derivation, we expressed $\tau_{\rm T}(k) = (kv_{\rm A})^{-1}$ and $\tau_{\rm nl} = (k\delta v_k) = k^{-3/2}E^{-1/2}$, where we used $\delta v_k \sim \sqrt{kE(k)}$ (Batchelor, 1982).

This scaling was the first phenomenological scaling for MHD turbulence. It was soon realized that the assumption of isotropic fluctuations, i.e., that the parallel $l_\parallel$ and perpendicular $l_\perp$ scales of the oppositely propagating Alfvén wave packets are the same $l_\parallel \sim l_\perp = l$, is violated. Montgomery and Turner (1981) and Shebalin et al. (1983) reexamined the interactions of the Alfvén waves in the so-called "weak" turbulence limit (sweeping is dominant). In this scenario, turbulence is comprised of an ensemble of weakly interacting Alvén waves with wave-vectors $\boldsymbol{k}$ and frequencies $\omega^{\pm}(\boldsymbol{k}) = \pm k_\parallel v_{\rm A}$. The cascade proceeds via resonant interactions of two oppositely propagating waves giving rise to a third wave. The resonant conditions are

$$\begin{aligned} \boldsymbol{k}_1 + \boldsymbol{k}_2 &= \boldsymbol{k}_3 \\ \omega^{\pm}(\boldsymbol{k}_1) + \omega^{\mp}(\boldsymbol{k}_2) &= \omega^{\pm}(\boldsymbol{k}_3). \end{aligned} \tag{2.34}$$

Shebalin et al. (1983) realized that the resonant conditions are nontrivial if either $k_{\parallel 1}$ or $k_{\parallel 2}$ equals zero. Therefore, the interactions inhibit parallel transfer of energy while the energy of waves with $k_\parallel$ cascades towards larger $k_\perp$, thus the fluctuations become anisotropic.

In order to obtain the scaling law for this regime, we evaluate eq. 2.30. Since the turbulence is "weak", the sweeping time controls the spectral energy transfer, thus $\tau_{\rm T} = \tau_{\rm A}(k_\parallel) \sim (v_{\rm A}k_\parallel)^{-1}$ and $\tau_{\rm nl}(k_\perp) = (k\delta v_k) = k_\perp^{-3/2}E^{-1/2}$ yielding $v_{\rm A}k_\parallel\epsilon = k_\perp^4 E^2(k_\perp)$. The perpendicular spectral scaling is therefore

$$E(k_\perp) \sim k_\perp^{-2}. \tag{2.35}$$

Goldreich-Sridhar $-5/3$ scaling

In the IK65 "weak" turbulent regime, the collisions of the Alfvén wave packets are brief and the change of the wave packet amplitudes during one collision is small. For the cumulative change to be comparable with the original amplitude, a number of collisions, N must be $N \gg 1$. However, Goldreich and Sridhar (1995) (hereafter GS95) suggested that below some scale, the turbulence cannot be considered "weak" anymore, and they introduced so-called *critical balance* expressed as

$$\tau_{\rm A}/\tau_{\rm nl} = \chi \quad \text{where} \quad \chi \sim 1 \qquad \Leftrightarrow \qquad \frac{l_\parallel}{l_\perp} \sim \frac{v_{\rm A}}{\delta v_l}, \tag{2.36}$$

implying that only one collision is sufficient for a significant distortion of the oppositely propagating wave packets. Therefore, there is only one natural time scale for the spectral energy transfer $\tau_{\rm T} = \tau_{\rm nl}$. Evaluation of eq. 2.30 yields the Kolmogorov scaling of the perpendicular fluctuations:

$$E(k_\perp) = \epsilon^{2/3} k_\perp^{-5/3}. \tag{2.37}$$

Observations in the solar wind

Observations within the heliosphere that span roughly half a century provide an overwhelming evidence of the turbulent cascade within the solar wind. A few of the most important observations were given in the previous chapter. Here, we focus on observations of the magnetic field, ion velocity, and ion density within the inertial range of scales. Power spectra of these *in situ* measured quantities could discriminate over the turbulent regimes presented above, but more importantly they tell us what real MHD turbulence really looks like.

In the text above, we often used wave-vector components (or spatial scales) parallel and perpendicular to *some* mean magnetic field $\boldsymbol{B}_0$. The question of how to define $\boldsymbol{B}_0$ arises therefore naturally. Since the magnetic field fluctuates significantly at the injection scales $L_{\rm i}$ and even in the inertial range, the orientation of the local average magnetic field would depend on the scale over which one estimate it, $\boldsymbol{B}_0 = \boldsymbol{B}_0(l)$. If we estimate the PSD of perpendicular magnetic fluctuations, it may not be sufficient to simply rotate the reference frame into one global $\boldsymbol{B}_0$ that is estimated over the span of the chosen data interval. Cho and Vishniac (2000) and Chen et al. (2011) showed that there are significant differences when analysing fluctuations using the global and local magnetic fields.

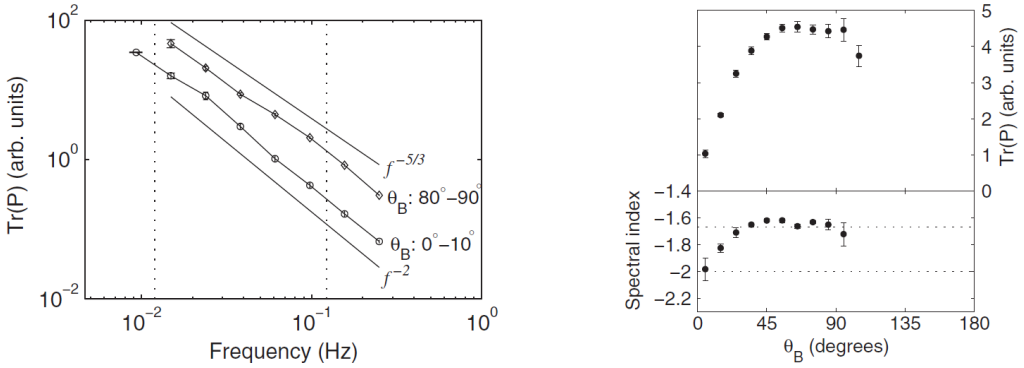

Figure 2.3: Left panel: Trace of the spectral matrix of the magnetic field fluctuations at two different angles between the local magnetic field and the solar wind flow $\theta_{\rm B}$. Right panel: trace of the power at 61 mHz as a function of $\theta_{\rm B}$ (top) and spectral index estimated in the frequency range of $15 - 93$ mHz as a function of $\theta_{\rm B}$. Adopted from Horbury et al. (2008).

For the sake of clarity, we distinguish between two kinds of anisotropy: (a) variance and (b) power anisotropies (Horbury et al., 2012). The former characterizes the ratios between the power within the perpendicular and parallel fluc-

tuations with respect to some mean magnetic field, $\boldsymbol{B}_0$:

$$\boldsymbol{B} = \boldsymbol{B}_0 + \delta B_\perp + \delta B_\parallel \quad \longrightarrow \quad var.\ anisotropy \sim (\delta B_\perp / \delta B_\parallel)^2. \tag{2.38}$$

On the other hand, the later represents the ratio of the total power P within the perpendicular $\boldsymbol{k} \perp \boldsymbol{B}_0$ and parallel $\boldsymbol{k} \parallel \boldsymbol{B}_0$ wave-vectors. By the total power, we mean the trace of the power spectral matrix, i.e.,

$$\begin{gathered} \boldsymbol{B} = \boldsymbol{B}_0 + \delta B_\perp|_{\boldsymbol{k}\perp\boldsymbol{B}_0} + \delta B_\perp|_{\boldsymbol{k}\parallel\boldsymbol{B}_0} + \delta B_\parallel|_{\boldsymbol{k}\perp\boldsymbol{B}_0} + \delta B_\parallel|_{\boldsymbol{k}\parallel\boldsymbol{B}_0} \\ P_\perp \sim \delta B_\perp^2|_{\boldsymbol{k}\perp\boldsymbol{B}_0} + \delta B_\parallel^2|_{\boldsymbol{k}\perp\boldsymbol{B}_0} \quad \& \quad P_\parallel \sim \delta B_\perp^2|_{\boldsymbol{k}\parallel\boldsymbol{B}_0} + \delta B_\parallel^2|_{\boldsymbol{k}\parallel\boldsymbol{B}_0} \\ pow.\ anisotropy \equiv P_\perp / P_\parallel \end{gathered} \tag{2.39}$$

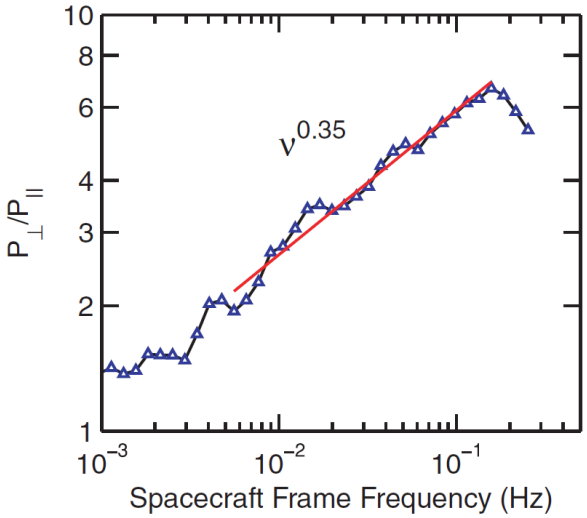

Figure 2.4: Power anisotropy, $P_\perp/P_\parallel$ as a function of the frequency. Image adapted from Podesta (2009).

Horbury et al. (2008) showed for the first time that the power anisotropy is indeed present in the solar wind. When sampling the solar wind in the direction perpendicular to the local magnetic field then the total power within the fluctuations is roughly 4-5 times greater than when sampling in the parallel direction[2]. Moreover, the scaling of the perpendicular and parallel power spectra match the prediction of the GS95 strong turbulence model, i.e., $P_\perp(f) = PSD(\delta B|_{\boldsymbol{k}\perp\boldsymbol{B}}) \sim f^{-5/3}$ and $P_\parallel(f) = PSD(\delta B|_{\boldsymbol{k}\parallel\boldsymbol{B}}) \sim f^{-2}$ (Figure 2.3). Furthermore, Podesta (2009) detailed the method based on a wavelet decomposition techniques devised by Horbury et al. (2008) and analyzed several long-duration high velocity streams using the STEREO A/B data. He concluded that although the measurements in the ecliptic plane do not yield reliable scaling laws, the power anisotropy scales with spacecraft frame frequency according to the GS95 theory, i.e., $P_\perp/P_\parallel \propto f^{1/3}$ (Figure 2.4).

On the other hand, the variance anisotropy, $(\delta B_\perp/\delta B_\parallel)^2$ is tightly connected

[2]At the spacecraft frame frequency of 61 mHz.

to the compressibility of fluctuations, $C_{\parallel} = (\delta B_{\parallel}/\delta B)^2$, via

$$(\delta B_{\perp}/\delta B_{\parallel})^2 + 1 = \frac{1}{C_{\parallel}}. \tag{2.40}$$

Since the inertial range is comprised mostly of the Alfvénic fluctuations for whose $\delta B_{\parallel} = 0$ in the MHD limit[3], one expects to observe high levels of the variance anisotropy within the inertial range. However, the solar wind does not consist solely out of shear Alfvén waves and slow mode fluctuations and/or pressure balance structures, which exhibit significant parallel fluctuations, are present also (McComas et al., 1995; Howes et al., 2012). TenBarge et al. (2012) reported that the average variance anisotropy within the inertial range is around 10 and that it is consistent with the solar wind containing 90/10 % of Alfvén/slow wave energy[4]. Furthermore, Smith et al. (2006b) analyzed hundreds of $\gtrsim 1$ hour long intervals recorded by the ACE spacecraft and showed that the variance anisotropy is a function of the proton beta, $(\delta B_{\perp}/\delta B_{\parallel})^2 \propto \beta_p^{-0.7}$.

Continuing the discussion of compressibility of the solar wind plasma, the parallel fluctuations of the magnetic field are tightly connected with the fluctuations of the density. Montgomery et al. (1987) showed that in the framework of nearly-compressible MHD turbulence, i.e., $\delta\rho/\rho_0 \ll 1$, density fluctuations should posses a Kolmogorov scaling $P_{\rho} \propto f^{-5/3}$, where P_{ρ} denotes the power spectrum density of density fluctuations. Earlier observations showed that this inertial range scaling is typical for the slow solar wind (Marsch and Tu, 1990) and it is slightly less steep for the fast solar wind. Šafránková et al. (2015) reported that the slope depends on the absolute level of the density fluctuations within the inertial range, namely σ_N, is the square root of the variance estimated over 20-min long spacecraft frame interval. For a moderately fluctuating solar wind $\sigma_N \lesssim 0.5$ cm^{-3} the scaling is close to $-5/3$, however, for large levels of σ_N the scaling is closer to -2.

2.3.3 Kinetic range

In the hydrodynamics, the range of scales where the turbulent energy is deposited into the system in a form of unorganized particle motions is usually denoted as the dissipation range and its spatial scale is defined in terms of the Kolmogorov (viscous) scale $l_{\mathrm{K}} = (\nu^3/\epsilon)^{1/4}$. In the MHD, a term *kinetic* is frequently used, because it highlights the fact that the ideal MHD no longer serves as an appropriate tool for the description of the sub-ion fluctuations and some form of a kinetic treatment is required.

The turbulent energy at the high wave-number end of the inertial range transforms into other form of energy, mainly the electron and ion thermal energies. How exactly does this collisionless process works is still an open fundamental problem in plasma astrophysics (Matthaeus and Velli, 2011). Some questions have been already addressed by many authors: (i) What scale/scales control the onset of the dissipation range of turbulence? (ii) What scaling laws the dissipa-

[3]Note that for collisionless Vlasov-Maxwell solutions for $\delta B_{\parallel}$ of the Alfveén mode is not a zero and it depends on $k_{\perp}$. For details, see, e.g., TenBarge et al. (2012).

[4]They measured variance anisotropy within one 5-day long data interval from STEREO A, compared it with Vlasov-Maxwell simulations, and got an excellent agreement.

tion range exhibits? (iii) What are the heating rates of electrons and protons? A high cadence of *in situ* plasma measurements allows to study the transition region between the inertial and kinetic ranges of turbulence. In a typical solar wind, the spacecraft frame frequency of this transition is around 0.5 Hz. Magnetic field measurements with Nyquist frequencies higher than $1 - 2$ Hz were analyzed in order to answer the first two questions (e.g., Leamon et al. (1998); Smith et al. (2006a); Alexandrova et al. (2008); Sahraoui et al. (2009); Chen et al. (2013), and many others).

A statistical study of Chen et al. (2014b) tooks advantage of the large amount of Wind data and they selected data intervals with extreme ion plasma beta ($\beta_{\rm p} > 10$ and $\beta_{\rm p} < 0.1$). They found that a transition from inertial to kinetic (dissipation) ranges occurs at larger of the ion gyroradius and ion inertial length scales, thus constraining a possible dissipation mechanism at ion scales. On the other hand, the Cluster spacecraft were successful in measuring turbulence between characteristic ion and electron scales. Alexandrova et al. (2009) and Alexandrova et al. (2012) analyzed 100 magnetic field power spectra and found that the power of the fluctuations decreases as a power law $P(f) \propto f^{-8/3}$ between the ion and electron scale, suggesting another turbulent cascade; furthermore, an exponential decrease below the electron scales was suggested.

Observations also show that the power anisotropy within the inertial range extends to the kinetic range, i.e., the turbulent eddies are elongated along the local magnetic field (Podesta, 2009; Chen et al., 2010). Two possible modes of kinetic plasma fluctuations that could exhibit such anisotropy are KAWs and whistler waves (see chapter 2.1.2). Observations over the past decade show that there is a satisfactory evidence that a transition from inertial to ion kinetic ranges and the kinetic range itself is composed of KAWs. Bale et al. (2005) showed that the electric field spectrum at $k\rho_{\rm gp} \gtrsim 1$ is consistent with the dispersion relation of short-wavelength KAWs. Furthermore, Chen et al. (2013) concluded that the compressibility of the kinetic range fluctuations (eq. 2.6) measured by the ARTEMIS spacecraft are consistent with KAWs rather than with whistlers. In their study, the density fluctuations were estimated from the spacecraft potential fluctuations, i.e., they are basically electron fluctuations. On the other hand, Šafránková et al. (2015) analyzed high-cadence ion density measurements from BMSW and showed that a plateau in the ion density power spectrum–frequently observed at the transition region from inertial to kinetic range–is consistent with the population of KAWs in this region (Chandran et al., 2009).

The slopes of the PSDs of magnetic field and density fluctuations estimated from measurements (Chen et al., 2013) and recent simulations (Boldyrev and Perez, 2012; Franci et al., 2015) suggest that the ion kinetic range could be characterized as strong KAW turbulence. Both phenomenology[5] (Boldyrev and Perez, 2012) and simulations (Franci et al., 2015, 2018) recover the spectral energy densities of δn and $\delta B_\perp$ as a function of perpendicular wave-number:

$$E(k_\perp) \propto k_\perp^{-8/3}. \tag{2.41}$$

[5]Note that in the original phenomenology of kinetic Alfvén turbulence (e.g., Schekochihin et al. (2009)), the predicted spectral law of perpendicular magnetic and density fluctuations are $E_B \sim E_n \propto k_\perp^{-7/3}$.

However, there are more possibilities that could explain the steep power spectra. Smith et al. (2012) suggested that ion-cyclotron damping instead of the KAW cascade could be present at a significant level. Howes et al. (2011) interpreted -8/3 magnetic spectrum in the gyrokinetic simulations as a signature of electron Landau damping. Rudakov et al. (2011) suggested that nonlinear scattering of KAWs by electrons leads to the steepening of the -7/3 slope into -8/3. For more details, see excellent review of Chen (2016) who summarized recent advancements in solar wind turbulence observations.

Finally, the question of heating rates of electrons and protons and their connection to turbulence were examined by Wu et al. (2013). They performed a fully electromagnetic particle-in-cell simulations and focused on the nature of the decay and the overall kinetic dissipation rate. They have found that for small/large turbulence amplitudes, electrons/protons are preferentially heated. This finding is consistent with the observations of the solar wind proton and electron temperatures, where the former are usually larger than the later.

2.3.4 Decay laws

First, let us briefly review the basic phenomenological model for the decay of HD turbulence. Although the topic is rich in history (Davidson et al., 2011), we will focus on the phenomenology of de Karman and Howarth (1938). Central to the phenomenology is the so-called *self-preservation hypothesis* that the correlation functions preserve their shape during the decay (Davidson, 2004). In the von Karman and Howarth phenomenology, it is the outer scale dynamics that control the decay of turbulent energy. The equations that govern the decay are

$$\frac{\mathrm{d}u^2}{\mathrm{d}t} = \alpha \frac{u^2}{\tau_{\mathrm{nl}}} \tag{2.42}$$

and

$$\frac{\mathrm{d}\lambda}{\mathrm{d}t} = \beta u, \tag{2.43}$$

where u^2 is twice the total energy per unit mass, α and β are positive constants of order unity and λ is the length scale of the largest eddies (correlation scale). For the choice of $\alpha = 1$ and $\beta = 1/2$, the asymptotic solutions ($t \gg t_0$) can be written as

$$u^2 \propto (t - t_0)^{-1} \tag{2.44}$$

and

$$\lambda \propto (t - t_0)^{1/2}. \tag{2.45}$$

These functional forms are observed in various experiments including wind tunnels (Batchelor, 1982).

The decay of MHD turbulence is much complex (Hossain et al., 1995), due to presence of the magnetic filed. In HD turbulence, the conserved quantities are the energy and kinetic helicity, but the later is considered of less importance (Kraichnan, 1973). In contrast, there are believed to be three so-called *rugged quadratic invariants* in ideal 3D MHD, i.e., integral quantities that are conserved in the absence of dissipation, $\mu = \nu = 0$. Namely, they are the total energy per

unit density E, the cross helicity H_c, and the magnetic helicity H_m defined as

$$E = E_\mathrm{k} + E_\mathrm{m} + \frac{1}{2}\int (\boldsymbol{v}^2 + \boldsymbol{b}^2)\mathrm{d}V \tag{2.46}$$

$$H_\mathrm{c} = \frac{1}{2}\int (\boldsymbol{v}\cdot\boldsymbol{b})\mathrm{d}V \tag{2.47}$$

and

$$H_\mathrm{m} = \int (\boldsymbol{A}\cdot\boldsymbol{B})\mathrm{d}V, \tag{2.48}$$

where E_k is the kinetic turbulent energy, E_m is the magnetic turbulent energy, $\boldsymbol{b}$ is the magnetic field in Alfvén speed units $\boldsymbol{b} = \boldsymbol{B}/\sqrt{\mu_0\rho_0}$ and $\boldsymbol{A}$ is the magnetic vector potential, $\boldsymbol{B} = \boldsymbol{\nabla}\times\boldsymbol{A}$ (see, e.g., Matthaeus and Goldstein (1982); Biskamp (2003)).

The complexity of the relaxation processes reveals itself when we realize that there is always some amount of dissipation present in the real physical system and that the invariants could decay with different rates, a process termed as *selective decay*. The two selective decay processes that are most widely studied are (i) relaxation to the minimum energy state under the constraint of constant magnetic helicity and (ii) relaxation to the minimum energy assuming slow decay of cross helicity and constant magnetic helicity. The first process gives rise to the linear force-free fields for which

$$\boldsymbol{\nabla}\times\boldsymbol{B} - \lambda\boldsymbol{B} = 0, \tag{2.49}$$

where λ denotes the Lagrange multiplier that is determined by the value of H_m. The second process leads to the the purely Alfvénic states for which

$$\boldsymbol{v} = \pm\boldsymbol{b}. \tag{2.50}$$

These states (eqs. 2.49 and 2.50) are long-time asymptotic equilibrium solutions because they cancel the nonlinear terms responsible for the turbulent dynamics (Matthaeus et al., 2012; Servidio et al., 2014).

Stribling and Matthaeus (1991) performed a large set of simulations in order to scan the parameter space defined by the rugged invariants and studied the asymptotic properties of the system with respect to various initial values of H_m and H_c. Figure 2.5 shows the evolution of the MHD system towards asymptotic states inferred from simulations. The asymptotic state depends on the initial value of normalized magnetic and cross helicity, $\sigma_\mathrm{m} = H_\mathrm{m}/E$ and $\sigma_\mathrm{c} = 2H_\mathrm{c}/E$, respectively.

These equilibrium solutions are often believed to appear at later stages of the turbulent evolution, i.e., in a long time and long length scale limit. However, both the simulations (Servidio et al., 2008; Matthaeus et al., 2008) and the solar wind observations (Servidio et al., 2014) show that patches of these local relaxation processes can be observed well before the termination of the turbulent cascade and can coexist with it.

Considering the freely decaying turbulence and finding a asymptotic solutions of kinetic and magnetic energies for various scenarios in a form of a power law $Energy \propto (t - t_0)^{-n}$, we adopt the phenomenologies listed in Biskamp (2003)

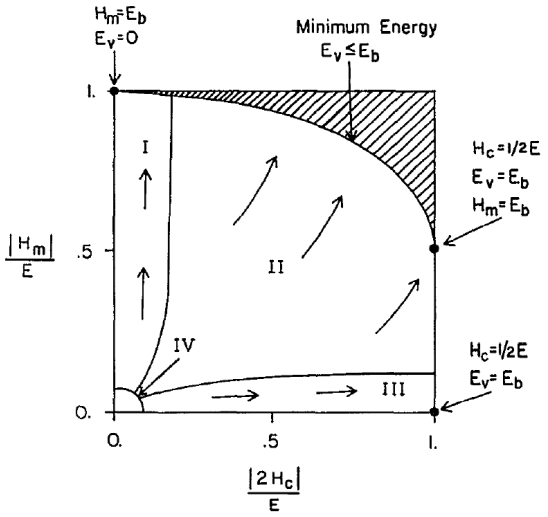

Figure 2.5: Sketch of evolution of the MHD turbulence within the parameter space $\{|H_\mathrm{m}|/E, |2H_\mathrm{c}|/E\}$. Adopted from Stribling and Matthaeus (1991).

and references therein.

Since the magnetic helicity is the rugged invariant that decays very slowly and for high Reynolds number it is well conserved, in most phenomenologies it is simply assumed to be a constant and it can be expressed as

$$H_\mathrm{m} = E_\mathrm{m} L_\mathrm{m} = \text{constant}, \tag{2.51}$$

where E_m is the magnetic energy and L_m is the magnetic integral scale. The values of exponents in the power law decay of total, magnetic and kinetic energies will strongly depend on the value of H_m.

First phenomenological decay law was predicted by Hatori (1984). Biskamp and Müller (1999) derived the same law using different approach: assuming self-similarity $E \sim E_\mathrm{m} \sim E_\mathrm{k}$, finite magnetic helicity and equating the integral and magnetic integral length scales. The decay law is $E \sim t^{-2/3}$. It turns out that this power law is not observed in simulations (Müller and Biskamp, 2003) due to the fact the similarity assumption (equal kinetic and magnetic energies) does not hold true in the decay, at least for finite magnetic helicity. When allowing the variable energy ratio $\Gamma = E_\mathrm{k}/E_\mathrm{m}$, following power laws can be derived:

$$E_\mathrm{m} \sim t^{-1/2} \tag{2.52}$$

and

$$E_\mathrm{k} \sim t^{-1}. \tag{2.53}$$

One can immediately see that the system is heading towards the static force-free state (eq. 2.49). This is a consequence of the inverse cascade of magnetic helicity (Frisch et al., 1975; Biskamp and Müller, 2000).

In the case of vanishing magnetic helicity $H_\mathrm{m} \simeq 0$, the decay proceeds towards Alfvénic state (eq. 2.50), i.e., the energy ratio is constant and kinetic and magnetic energy decays similarly:

$$E_\mathrm{m} \sim E_\mathrm{k} \sim t^{-1}. \tag{2.54}$$

Notably, Frick and Stepanov (2010) performed a large Reynolds number simulations using a shell model of turbulence. They studied nonhelical turbulence with small levels of cross helicity, $|H_{\rm m}| \lesssim 10^{-4}$, $|H_{\rm c}| \lesssim 10^{-4}$ and find that the system exhibits two types of evolution for the similar initial conditions. In the first scenario, the system quickly reaches the state with $\sigma_{\rm c} = \pm 1$ and some constant value of magnetic helicity. In the second scenario, the final state is highly helical with arbitrary level of $\sigma_{\rm c}$.

Considering the observations, it proves to be difficult to estimate the decay laws and their power law exponents from *in situ* measurements. The best case in the solar wind would be if one would have simultaneous multi-point observations along the solar wind flow at various distances from the Sun. This seldomly happens, therefore some kind of simplification and various assumptions have to be made in order to move forward. For example, Podesta (2006) analyzed solar wind data from Voyager and Helios spacecraft and found that the radial decay of the total energy seems to follow a power law with an exponent of $\sim -1/2$, whereas the kinetic energy decreases more rapidly for distances between 1 and 20 astronomical units, being consistent with the simulations by Biskamp and Müller (2000). However, at the distances between 0.3 and 1 AU, kinetic energy decays more gradually than magnetic energy. We will show that Pitňa et al. (2017) found that the decay of kinetic and magnetic energy obeys a power law with the same exponent of ~ -1.2, characteristic for turbulent systems with small magnetic helicity, in distances $R \leq 1$ AU.

Chapter 3

Aims of the thesis

In previous sections, we reviewed the broad topic of astrophysical plasma turbulence for conditions relevant to the solar wind. However, many concepts that have been outlined are valid for a wider range of physical parameters, i.e., the dimensions of the system, characteristic spatial and temporal scales of turbulent fluctuations, amount of free energy within the system, etc. By understanding the solar wind turbulence through observations and modeling–both simulations and theory–we will fathom the processes that govern a much wider range of systems than those of the solar wind itself.

A careful comparison of the observations and the theoretical concepts that supports them is central to this understanding. Within the last decades, the theory of inertial and, more recently, kinetic range of turbulence has been developed by many authors, and instruments onboard the dedicated spacecraft were able to measure the physical quantities of the turbulent flow with either (a) high sampling rate and/or (b) long data coverage. Two spacecraft that stand out, are NASA's Wind and Russian Spektr-R scientific satellites. The data acquired by the instruments onboard these spacecraft (SWE and MFI at Wind; BMSW at Spektr-R) make up a core of the thesis.

By exploiting the simultaneous measurements of these spacecraft, we can investigate solar wind fluctuations at both inertial and kinetic ranges, spanning 7+ years of intermittent concurrent observations. The main tasks of the thesis can be formulated as: (1) what changes in inertial and kinetic ranges of turbulence are induced by the passage of an interplanetary shock. As it was shown above, the energy within the inertial range fluctuations is enhanced by the shock. (2) What is the evolution of the enhanced energy further downstream the shock? (3) Using high-cadence density and velocity measurements of the BMSW instrument, we can study the kinetic range fluctuations. Can we combine these with the measurements of the magnetic field in order to address the question which plasma mode is dominant around the characteristic proton scales?

The techniques we applied in the analysis of the data were manifold. Among standard curve-fitting procedures where Levenberg-Marquardt algorithm can be employed, principal calculations required to find a power spectrum densities of various quantities. For this purpose, decomposition of a signal based on a continuous wavelet transform was employed. Finally, Monte Carlo techniques were also utilized.

Chapter 4

Analysis techniques

In this chapter, the techniques that have been used in the data analysis will be introduced. The focus is put on the signal processing with respect to the second and higher order spectra, which are intimately linked to phenomenological descriptions of the turbulent flows (power spectrum). A ubiquitous Fourier Transform (FT), namely its discrete form (DFT) implemented mostly through the Fast Fourier Transform (FFT) algorithm, has been used for decades. However, in recent years, Wavelet Transform has gain much popularity, due to its superior performance in the power spectra estimation and generally, in the processing of non-stationary signals. Therefore, the Power Spectral Densities (PSDs) of quantities were calculated using these techniques.

4.1 Wavelet analysis

In the spectral analysis of space plasma data, specifically the PSD estimation and time-frequency analysis, two common options are the Fourier or Wavelet techniques (Paschmann and Daly, 1998). In the Fourier analysis, the signal $u(t)$ is transformed into different sets of basis functions, namely, sines and cosines, $\tilde{u}(f)$. This transformation allows us for an easy identification of intrinsic frequencies in the signal that helps to understand the physical processes governing the system. However, if the process is non-stationary, thus the level of fluctuations at some frequencies changes with time, a time-frequency analysis should be adopted. For Fourier techniques, the most common approach is to divide a whole signal into smaller overlapping parts and compute the Fourier transform on each of them, thus providing the so-called dynamic spectrogram (power within the fluctuations in a time-frequency domain). The downside of this approach is that it makes impossible to identify the fluctuations with the lowest frequencies that could be present in the original signal, while the fluctuations with the highest frequencies remain poorly spatially identified. Generally, a signal sampled at the frequency f_s with N records, the frequency resolution $\Delta f = f_\mathrm{s}/N$ and time resolution $\Delta t = N/f_\mathrm{s}$, obey the inequality

$$\Delta f \Delta t \geq 1. \tag{4.1}$$

On the other hand, in the Wavelet techniques, the signal $u(t)$ is transformed into a set of basis functions that are both frequency and spatially localized, thus

they are uniquely suited for an analysis of any non-stationary signal. Wavelet techniques cannot avoid the time-frequency uncertainty principle introduced by eq. 4.1, rather, they take advantage of it. Generally, a condition $\Delta f/f = constant$ is obeyed, thus the components of the signal with higher frequencies are better spatially localized.

Formally, the wavelet transform of a function $u(t)$ can be defined as

$$W^u_\Psi(a,b) = \frac{1}{\sqrt{b}} \int_{-\infty}^{+\infty} u(t) \Psi^* \left(\frac{t-a}{b} \right) dt, \quad \text{where} \quad a \in \mathbb{R}, b \in \mathbb{R}^+, \tag{4.2}$$

Ψ is the wavelet mother function ($*$ marks the complex conjugate), b is the scaling (or dilation) parameter. The mother function Ψ satisfy the so-called admissibility condition [Louis et al. 1994] that leads to

$$\int_{-\infty}^{+\infty} \Psi(t) dt = 0, \tag{4.3}$$

i.e., it exhibit a zero mean. Moreover, $||\Psi|| = 1$.

There are infinite possibilities in choosing the mother function for the transform. Therefore, the choice is motivated by the physical underpinnings of the problem in question. For example, if one identifies discontinuities within the signal, Haar [1] wavelet is a good choice. If the signal is thought to be wave-like (as a consequence of the underlying linear or nonlinear physical processes), then the family of Morlet wavelets are commonly used (Torrence and Compo, 1998; Dudok de Wit et al., 2013).

Throughout the thesis, the Morlet wavelet[2] was adopted in the PSD estimation through Continuous Wavelet Transform (CWT). The Morlet wavelet is defined as

$$\Psi_0(\eta) = \pi^{-1/4} e^{i\omega_0 \eta} e^{-\frac{1}{2}\eta^2}, \tag{4.4}$$

where ω_0 is dimensionless frequency and η is dimensionless time. As in the most studies of solar wind turbulence, we chose $\omega_0 = 6$.

CWT of an equally sampled signal (time series) $u_n, n = 0, ..., N-1$ with time spacing δt, can be expressed as

$$W^u(n,s) = \sqrt{\frac{\delta t}{s}} \sum_{n'=0}^{N-1} u_{n'} \Psi_0^* \left(\frac{(n'-n)\delta t}{s} \right), \tag{4.5}$$

where n denotes the localized index and s denotes the wavelet scale. The wavelet scale is associated with the Fourier frequency ν_F via

$$\nu_F \simeq \frac{\omega_0}{2\pi s}. \tag{4.6}$$

[1] Haar wavelet is defined as

$$\Psi(t) = \begin{cases} 1 & \text{if} \quad 0 \le t < 1/2 \\ -1 & \text{if} \quad 1/2 \le t < 1 \\ 0 & \text{otherwise} \end{cases}$$

[2] Actually, the equation 4.4 is only an approximation of the true Morlet wavelet that reads $\Psi_0(\eta) = \pi^{-1/4} e^{-\frac{1}{2}\eta^2} \left[e^{i\omega_0 \eta} - e^{-\frac{1}{2}\omega_0^2} \right]$. For $\omega_0 = 6$, the second term in the brackets is negligible and it is usually omitted which leads to eq. 4.4.

The scales in eq. 4.5 can be chosen arbitrarily, however, it is convenient to write them in the fractional powers of two. Following Torrence and Compo (1998), we set the scales as

$$s_j = s_0 2^{j\delta j}, \quad j = 0, ..., J, \quad \text{where} \quad J = \frac{\log_2\left(\frac{N\delta t}{s_0}\right)}{\delta j}, \tag{4.7}$$

where s_0 is the smallest resolvable scale estimated from eq. 4.6 by substituting for ν_F the Nyquist frequency of the time series. Adequate scale sampling for the Morlet wavelet is $\delta j \sim 0.5$, but for a better resolution, $\delta j = 0.125$ is used.

Considering the definition of a wavelet power spectrum, a natural choice is to square the norms of each wavelet coefficient given by eq. 4.5

$$P_W(n, s) = |W^u(n, s)|^2 . \tag{4.8}$$

By displaying this quantity in the time-scale plane, the so-called wavelet *scalogram* is obtained. Furthermore, for a complex wavelet such as Morlet, wavelet coefficients contain information about the phases of the localized wave-packets and a *wavelet phase spectrum* can be defined as

$$\Phi_W(n, s) = \tan^{-1}\left[\frac{Im\{W^u(n, s)\}}{Re\{W^u(n, s)\}}\right] . \tag{4.9}$$

Finally, a *global wavelet spectrum* is defined [Torrence and Compo 1998] as an average of the wavelet power spectrum over time:

$$P_W(s) = \frac{1}{N}\sum_{n=0}^{N-1} |W^u(n, s)|^2 . \tag{4.10}$$

In the summation, wavelet coefficients that suffer from the edge effects are not taken into account.

Chapter 5

Instruments and data description

In the pursue of our understanding of plasma processes in the near Earth environment, many spacecraft have been launched and their data products have been analyzed. With the development of new technologies, less noisy and high cadence data can now be acquired (Spektr-R, MMS, Parker Solar Probe, Solar Orbiter). Although the data products have already been mined in depth and many findings have been made, the vast databases of data still offer an opportunity to made new discoveries. One of the spacecraft that offers near-continuous time coverage of solar wind plasma quantities is the *battle-star Galactica* among the NASA spacecraft, Wind. Second, high-time resolution of ion plasma moments from Spektr-R provides an excellent opportunity to study the sub-ion scale plasma fluctuation. In this work, the data mainly from these two satellites will be analyzed, therefore, more detailed descriptions of some of their instruments follow.

5.1 Spektr-R spacecraft

The Spektr-R satellite was launched on July 18, 2011. Its main purpose was to study the distant radio sources with high angular resolution through interferometry techniques. With a conjunction with ground base radio telescopes, an angular resolution could reach millionths of an arcsecond. It has an highly eccentric elliptic orbit with an apogee of $\sim$ 350,000 km and perigee of $\sim$ 10,000 km with orbital period of $\sim$ 8 days. Due to its orbit, Spektr-R contains also a science payload of PLASMA-F. It was designed for a study of the outer magnetosphere and solar wind. It consists of the energetic particle spectrometer MEP-2, the magnetometer MMFF[1], the solar wind monitor BMSW and the processing unit. BMSW samples the solar wind with high cadence, and its measurements provide a key data products that have been analyzed in this thesis.

5.1.1 BMSW

In order to estimate the main physical quantities of the solar wind plasma from the FCs measurements, many assumptions have to be made and a few problems have to be solved. BMSW consists of six Faraday's Cups (FCs) that collect the incoming flux of positively charged particles. Each FC is equipped with a grid

[1]Unfortunately, the magnetometer is not operational.

powered by a negative potential of $\sim -300\ V$ which reflects the incoming solar wind electrons and prevents the photoelectrons emitted from the collector by a solar UV photons from escaping. The residual current caused by photoelectrons emitted from the grid must be subtracted from the total measured current. Assuming an isotropic Maxwellian distribution of the solar wind protons, we need to perform at least five independent measurements in order to theoretically compute five physical quantities— density, three components of velocity vector and proton thermal velocity (temperature). Configuration that achieves this goal can be briefly described as follows: (a) three FCs with parallel axis oriented along the X axis of the instrument pointing approximately towards the Sun—group A, (b) three FCs inclined by 20° from the X axis of the instrument—group B—(see Figure 5.1). Moreover, control grids of the FCs of group A (FC0,FC1,FC2) are connected to a tunable HV source that can sweep the solar wind ions up to 3 kV, whereas control grids of the FCs of group B (FC3,FC4,FC5) are grounded. Estimation of the solar wind parameters can be schematically divided into two

Figure 5.1: A photograph of an engineering model of the BMSW instrument. Adopted from Šafránková et al. (2013a).

subsequent parts: (1) estimation of the total ion flux vector and the ratio of the thermal and bulk velocities, K, from the one FC from group A and all FCs from group B and (2) estimation of the bulk and thermal speeds using the measured deceleration (FC-HV) characteristics of the FCs from group A.

Following Šafránková et al. (2013a), a more detailed description of the processing of the measured FC currents and the applied voltages reads: (1) the measured current densities J_i, where i denotes the index of the particular FC, can be expressed as

$$J_\mathrm{i} = enV f_\mathrm{j}(\alpha_\mathrm{i}, K_1) \quad \text{for} \quad i = 2, 3, 4, 5 \quad \text{and} \quad j = 0, 3, \tag{5.1}$$

where f_j are functions defined by the FC geometry, e is the elementary charge and α_i are the angles between the solar wind flow and the axis of the FC. The cone and clock angles of solar wind speed in the reference frame of the instrument, θ

and ϕ, respectively, are expressed as

$$\begin{aligned} \alpha_{\mathrm{i}} &= \theta \qquad\quad \text{for} \quad \mathrm{i} = 0, 1, 2 \\ \alpha_{\mathrm{i}} &= \alpha_{\mathrm{i}}(\theta, \phi) \quad \text{for} \quad \mathrm{i} = 3, 4, 5 \end{aligned} \tag{5.2}$$

Functions f_{j} were estimated as polynomial fits of the 4th order in variables α and K of the model characteristics computed by the SIMION software package (for details see Šafránková et al. (2013a)). The numerical solution of the system of equations above yields four independent quantities: nV,θ,ϕ and K.

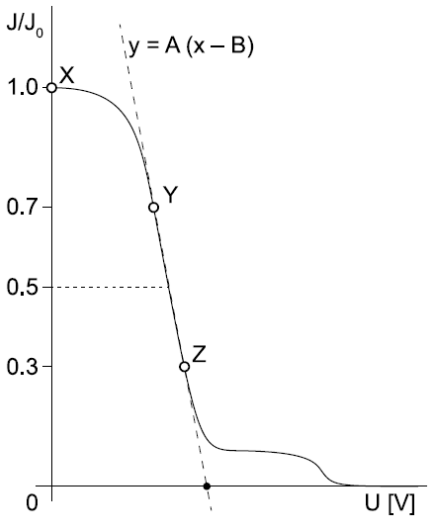

Figure 5.2: A sketch of the FC-HV characteristic and a graphic representation of the auxiliary variables A and B. Adopted from Šafránková et al. (2013a)

In order to find the bulk and thermal velocities, characteristics of FC0 and FC1 are processed as it follows: we define two auxiliary variables, A and B (see Figure 5.2). A is defined as a first derivative of the FC-HV characteristic at a point where the FC current J is equal to half the current of that of FC2 ($J/J_0 = 0.5$), i.e, FC with zero potential. Variable B is defined as the intersection of the voltage axis with a line that goes through the point where $J/J_0 = 0.5$ and has the slope A. Analysis of the modeled FC characteristics yields the following simplified equations that couple A and B with the energy $E = 1/2 m_{\mathrm{p}} V^2$, K and θ:

$$\begin{aligned} A &= \tfrac{1}{E} g(K, \theta) \\ B &= E h(K, \theta) \end{aligned} \tag{5.3}$$

where g and h are the modeled function estimated from the simulated FC characteristics. Numerical solutions of these equations yield values of E and K. Expressing the bulk and thermal velocity follows trivially.

Note that in both (1) and (2) parts above we obtained value of K. They should be equal, however, due to the small imprecisions in manufacturing, instrumental and plasma noises, the values are slightly different (difference is less than 10 %). Because K depends more strongly on A and B, in the final calculation of velocities, K from the second part of the calculation is used.

Importantly, the instrument can operate in sweeping or adaptive modes. In the former, a sweeping saw-tooth voltage (0-3 kV) on FC0 and FC1 is applied.

A duration of each sweep can vary (1.5, 3 or 6 seconds). Since FC2 is grounded, the final resolution can be $\sim\ 0.75 - 1.5$ s. This mode produces a 1D-energy distribution and can detect both protons and alpha particles (Šafránková et al., 2013a). On the other hand, in the adaptive mode, the voltage on FC0 and FC1 is adjusted via feed-back loops to depress their collector currents to 0.3 and 0.7 fraction of the FC2 collector current. In this mode, the line defined by variables A and B (see eq. 5.3 and Fig. 5.2) is simply the line that goes through the both points (X and Y) of the FC-HV characteristics. A time-resolution of this mode is 32 ms and therefore solar wind parameters estimated in this mode are suitable for the analysis of the kinetic range turbulence within the solar wind.

5.2 Wind spacecraft

Wind, a spin stabilized spacecraft, was launched on November 1, 1994. After almost quarter of a century/two solar cycles, it remains operational and still provides an excellent data that produce new exciting results. Since the deployment, its orbit was rather chaotic, due to the study of magnetosphere processes and the near lunar environment. In May 2004, it was brought to its final orbit around the L1 Lagrange point and remained there until know.

Instrument	Measured quantities	Cadence [s]
MFI[1]	DC vector magnetic field	0.09/0.045
SWE[2]	p^+, α^{2+} & e^- N, T, $\boldsymbol{V}_{sw}$; e^- distribution	92/12
3DP[3]	p^+, α^{2+} & e^- N, T & $\boldsymbol{V}_{sw}$	3
WAVES	FFT $\boldsymbol{E}, \boldsymbol{B}$, N_{e^-}	60
EPACT[4]	SEP[5] intensities	300
KONUS & TGRS[6]	Fluxes of p^+ & e^- in 20 keV—15MeV	8/0.25
SMS[7]	$M, Q, M/Q, E, isotopic\ abundances$	14400/180

Table 5.1: Brief description of the instruments onboard the Wind spacecraft. [1]Magnetic Field Investigation. [2]Solar Wind Experiment. [3]3D Plasma analyser. [4]Energetic Particles: Acceleration, Composition and Transport investigation. [6]Solar Energetic Particles. [6]Transient Gamma-Ray Spectrometer. [7]**S**TICS-**M**ASS-**S**WICS denotes SupraThermal Ion Composition Spectrometer-mass spectrometer-Solar Wind Ion Composition Spectrometer.

Brief characteristics of the onboard instruments are shown in Table 5.2. The most important instruments for the study of solar wind turbulence are MFI and SWE. In combination, all macroscopic quantities relevant for the inertial range turbulence can be calculated, i.e., energies within the magnetic and velocity fluctuations, cross-helicity, residual energy, Alfvén ratio, etc. However, the kinetic range fluctuations can only be measured by MFI. Since the magnetic field and ion measurements from MFI and SWE were used in the thesis, a short description of these instruments follows.

5.2.1 MFI

MFI consists of two triaxial fluxgate magnetometers each mounted on a 12 m long boom. Due to the importance of the magnetic field measurements, the whole instrument is fully redundant in order to minimize the possibility of a failure. In a standard mode, it provides nearly continuous DC magnetic field vector measurements with a nominal resolution of 0.092 s (11 Hz) in GSE and GSM coordinate systems whereas the total r.m.s. noise level over the 0—10 Hz band is lower than 0.006 nT (Lepping et al., 1995).

5.2.2 SWE

SWE consists of the following instruments: two Faraday Cups (SWE-FC),a Vector Electron and Ion Spectrometer (VEIS), a strahl sensor and onboard calibration system (Ogilvie et al., 1995). Measurement of the protons and alpha particles by the SWE-FC subsystem provide a comprehensive set of physical quantities that includes parallel and perpendicular temperatures of both protons and alpha particles together with their velocities and densities. Nominal resolution of these data sets are $\sim$92 s. Kasper et al. (2006) showed that the uncertainty of the key parameters, $N, V_{\rm sw}$ and T, is 0.8%, 3.6% and $< 9\%$, respectively.

Chapter 6

Interplanetary shocks and turbulence

In this chapter, we present three separate analyses of the turbulent solar wind fluctuations. First of them addresses changes of small and large scale fluctuations induced by the passage of an interplanetary (IP) shock and the second is dedicated to a long term evolution of inertial range fluctuations. Finally, the third analysis focusses on the nature of small scale fluctuations in the pristine solar wind. The first and second studies take advantage of the fact that IP shocks enhance the level of fluctuations, which in turn allows us (1) to study the immediate changes induced by an IP shock and (2) to observe a decay of large scale fluctuations in time.

6.1 Upstream and downstream fluctuations

A propagation of a shock wave in an unionized medium has been studied for decades and it is a well-understood phenomenon (Krehl, 2007). Generally, a shock forms when either (a) an obstacle is put into a super-sonic flow or (b) the obstacle moves faster than a local sound speed. These situations are equivalent and they differ only by the frame of reference. In fluids where the dissipation is mediated through binary collisions, the shock front has a width of the order of the collisional mean free path, therefore it is basically a discontinuity. The medium into which the shock propagates is referred to as *upstream*, whereas the medium that is behind the shock front as *downstream*. Because the shock front stands in some distance from the obstacle, the sound speed in the downstream medium must be lower than the speed of the this medium relative to this obstacle, in order for the information that there is an obstacle in the way of the flow to be transmitted to the shock front. This implies that the downstream temperature is higher than the upstream one, thus the thin shock front is generating an entropy, which makes the whole process irreversible (Balogh and Treumann, 2013). Flux conservation leads to increasing density across the shock, implying an increase in pressure. The changes in bulk parameters of the fluid (density, N, speed V, temperature, T) from upstream to downstream medium are governed by the Rankine-Hugoniot relations.

Shocks in magnetized plasmas are more complex, partly due to an existence of several wave modes with different group velocities and partly because the plasmas

could be collisionless. Here, we will not describe an extensive nomenclature of all the possible types of shock. We will only briefly introduce the most common type of an IP shock that can be encountered within the solar wind: a supercritical fast-magnetosonic quasi-perpendicular IP shock. The term *quasi-perpendicular* refers to the angle, θ_{Bn} between the shock normal, $\boldsymbol{n}$ and the upstream magnetic magnetic field vector, $\boldsymbol{B}_u$. Quasi-perpendicular shocks have $\theta_{Bn} > 45°$. The term *fast* refers to MHD wave modes (slow, fast or intermediate) that is relevant for the shock formation. This translates into a condition that the upstream velocity of the medium, $V_{\rm up}$ must exceed the speed of the fast magnetosonic wave, $c_{\rm fms}$. This condition is usually expressed as $\mathcal{M}_{\rm cms} > 1$, where $\mathcal{M}_{\rm cms} = V_{\rm up}/c_{\rm fms}$ is the so-called (magnetosonic) Mach number. Finally, the *supercritical* refers to a class of shocks whose Mach numbers exceed some critical Mach number $\mathcal{M}_{\rm c}$ (Balogh and Treumann, 2013). The physical difference from the subcritical shocks ($\mathcal{M}_{\rm cms} < \mathcal{M}_{\rm c}$) is in the dissipation mechanism within the shock front. On top of the anomalous dissipation which is sufficient for subcritical shocks to support the shock front, the supercritical shocks reflect part of the incoming particles back into the upstream medium. Importantly, the upstream medium of supercritical shocks differ drastically between quasi-parallel and quasi-perpendicular IP shocks. It turns out that the angle $\theta_{Bn} = 45°$ that distinguishes the two types of oblique shocks is quite a sharp limit with respect to the fate of the reflect particles. For quasi-perpendicular geometry, the reflected particles are confined within a few gyroradii near the shock front. However, for quasi-parallel geometry, the reflected particles can propagate deeply into the upstream medium and can create a so-called *foreshock* region.

As it was mentioned, supercritical fast-magnetosonic quasi-perpendicular IP shocks are the most common type of shocks within the solar wind, therefore we limit our discussion to them. Since the IP shocks are propagating within a turbulent medium, their interaction with this medium attracts much attention and therefore it has been studied by many authors but the majority of studies were focussed on transport equations and/or particle acceleration from a theoretical perspective [i.e., Zank et al. (2006); Sokolov et al. (2009); Dosch and Shalchi (2010).

Nature of MHD and kinetic fluctuations immediately upstream and downstream of quasi-perpendicular IP shocks were studied scarcely. Luttrell and Richter (1987) investigated magnetic field, velocity and density fluctuations in the frequency range 10^{-4}–10^{-2} Hz associated with fast forward oblique IP shocks. They found that the spectral densities were on average 13 times higher in the downstream region. Similarly, Lu et al. (2009) showed through self-consistent two-dimensional hybrid simulation of interaction of Alfvén waves with a perpendicular shock that the amplitude of a wave is enhanced 10-30 times. They verified their simulation results by an observation of one quasi-perpendicular fast forward IP shock.

Due to the lack of a systematic studies analyzing both the upstream/downstream MHD/kinetic fluctuations at quasi-perpendicular fast forward IP shocks, Pitňa et al. (2016) analyzed 34 IP shocks with a focus on the shape of the power spectra of ion flux fluctuations. We analyzed shocks registered at Spektr-R between 2011 and 2014 that met the following criteria:

1. fast forward shock

2. data cover at least 22 minutes both upstream and downstream of the shock front

3. the percentage of missing data is less than 5%.

In order to exclude a possible whistler wave activity near the shock front (Němeček et al., 2013; Goncharov et al., 2014), we discarded 2 minutes immediately upstream and downstream of the shock ramp. The upstream and downstream power spectra densities (PSDs) were estimated via Fast Fourier Transform (FFT). Figure 6.1a shows the upstream and downstream PSDs of the ion flux for each IP shock, whereas Figures 6.1b and 6.1c shows the average of the upstream and downstream spectra and their ratio, respectively. The ratio shows that the power within the fluctuations in the MHD range increases roughly by a factor of 20 without any significant frequency dependence. However, the change in the power of kinetic range fluctuations is more complex. The ratio of downstream and upstream PSD for each case exhibits a peak located at the frequency f_p. It follows that the downstream PSDs above the f_p are steeper than the upstream PSDs. Figure 6.2a shows that this is indeed the case. Moreover, the upstream and downstream slopes in the kinetic range above the f_p are highly correlated. As it can be seen from Figure 6.1a, the power of the downstream fluctuations is almost always higher than that of the upstream fluctuations. Thus, the steeper kinetic range spectra could be connected with the fluctuation levels in the MHD range. Figure 6.2B shows that the standard deviation of the ion flux computed in the same intervals as PSDs, is anti-correlated with the kinetic range slope.

Spectra of the kinetic range fluctuations depicted in Figure 6.1a and 6.1b show that the upstream power spectra can be reasonably characterized as two power laws connected at a break frequency f_b. Let us denote this phenomenological function as "bp". However, the downstream spectra exhibit a varying degree of curvature, which suggests that the bp model may not characterize these spectra well. Pitňa et al. (2016) followed the approach of Spangler and Gwinn (1990) and fitted the power spectra with a phenomenological model function, so-called exponentially truncated power law, defined as

$$g(f) = a \cdot f^b \cdot e^{\left(\frac{f}{f_0}\right)}, \tag{6.1}$$

where a,b and f_0 are parameters of the fit. We denote this function as "pe". In order to estimate which model function fits the kinetic scale spectra better, reduced χ^2 was used for a qualitative assessment of the goodness of the fit. Figure 6.3 shows the χ^2_bp as a function of χ^2_pe, where the subscripts denotes the reduced χ^2 of the two model functions. One can see that all upstream PSDs are reasonably characterized by a "bp" function. In contrast, approximately 1/2 of the downstream PSDs are better fitted by an exponentially truncated power law function (see region I in Figure 6.3).

From these and other observations, Pitňa et al. (2016) concluded that while the passage of an IP shock increases the power within the inertial range fluctuations of turbulence, the slope of the spectra are not affected, which suggests that the properties of the turbulent cascade are conserved across the shock. The authors suggest that the exponential decay in the kinetic range can be caused by a strong damping.

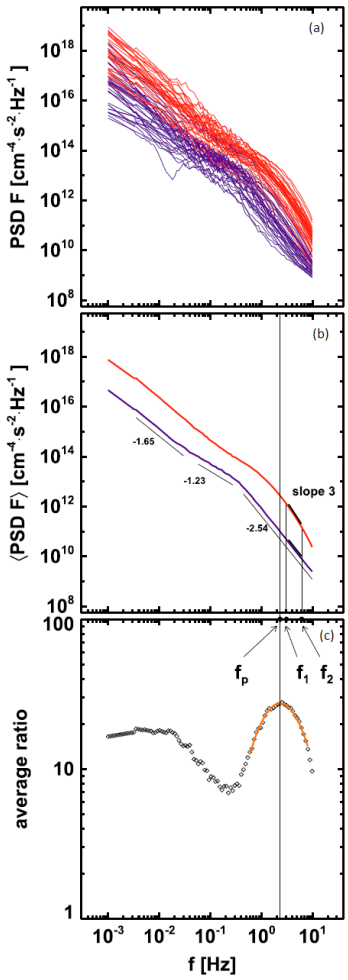

Figure 6.1: (a) Summary plot of all upstream (blue) and downstream (red) frequency spectra; (b) median values of PSD upstream and downstream of the shock; (c) ratio of downstream to upstream PSDs. See Pitňa et al. (2016) for a definition of f_p, f_1, f_2, and slope 3. Adopted from Pitňa et al. (2016).

Although the role of the KAW were not discussed in the paper, it is instructive to interpret these findings through the KAW optics. KAW waves are believed to play a dominant role in the dynamics of the kinetic scale fluctuations. Kinetic range turbulent models involving KAW (Schekochihin et al., 2009; Boldyrev et al., 2013) predict the same scaling of perpendicular magnetic field and density fluctuations $E(k_\perp) \propto k_\perp^{-8/3}$ (eq. 2.41). The spectral scaling of $-8/3$ is consistent with the slopes of the kinetic range fluctuations in the upstream region. However, the steeper slopes (Figure 6.2b) and, more importantly, the curvature of the spectra in the downstream region (Figure 6.3) suggest that the KAW turbulent cascade is either (a) not present or (b) it is present, but other fluctuation modes are dominant. Considering the former, the fluctuations still could be characterized as KAW-like, but the power law spectrum is not formed due to an enhanced damping. KAW normalization introduced by Chen et al. (2013) and further extended by Pitňa et al. (2019) should provide more evidence and could discriminate between the two possibilities.

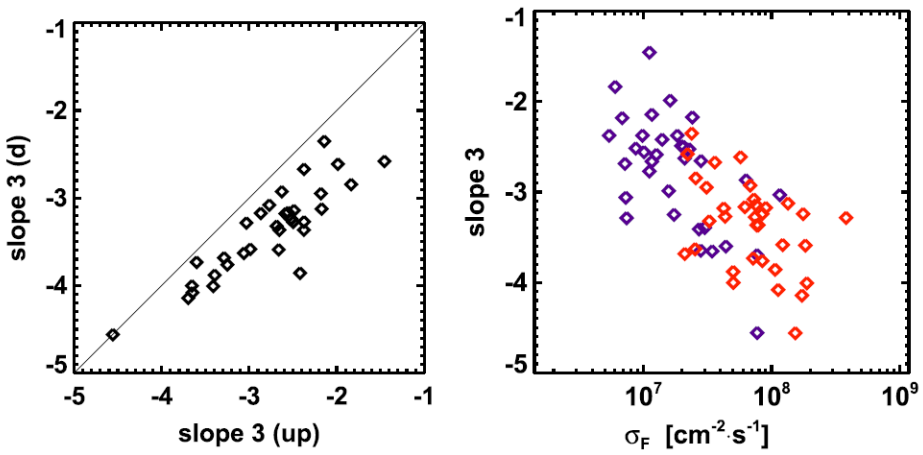

Figure 6.2: Spectral slopes in upstream and downstream regions. (left plot) Slope 3 in the downstream region as a function of the corresponding slope upstream (correlation coefficient, $C = 0.83$). (right plot) Slope 3 as a function of the ion flux standard deviation ($C = -0.69$). The red and blue symbols indicate the upstream (blue) and downstream (red) spectra, respectively, and corresponding standard deviations. Adopted from Pitňa et al. (2016).

6.2 Long-term evolution of fluctuations after the shock passage

In this section, we focus on the decay of the turbulent fluctuations after the passage of an IP shock. As it was shown in previous section, the level of fluctuations is enhanced, i.e., the inertial range fluctuations in the downstream region contains more free energy than the fluctuations in the upstream region. This energy is constantly transferred via turbulent cascade into kinetic scale fluctuations where it is dissipated. Thus, in the absence of the forcing, the inertial range fluctuations will decay in time.

In solar wind, the majority of the forcing takes place in the solar corona and acceleration region, i.e., it is active close to the Sun. On top of that, IP shock fronts effectively serve as additional sources of turbulent energy. Naturally, this source is active as long as the shock is maintained. Because the downstream region is free of sources for of turbulent fluctuations, one can look at this region as a natural laboratory for a study of the MHD turbulence decay.

Before we show how one can exploit 1 AU measurements for a study of the turbulence decay with the help of IP shocks, we list other possibilities. Perhaps the most feasible and the most accurate way how to investigate the decay in the solar wind would be to simultaneously measure the fluctuations at multiple distances from the Sun. Bruno et al. (2009) proposed a coordinated study of solar wind at the end of August 2007, when Venus, Earth and Ulysses had been aligned. In turn, D'Amicis et al. (2010) analyzed the measurements of ACE (1 AU) and Ulysses (1.4 AU) in the suggested time period. During the alignment, ACE and Ulysses observed a stream of slow solar wind, a compression region ahead of the fast solar wind stream, and a high speed stream (HSS) itself. They estimated the PSDs of magnetic field fluctuations within the HSS on both locations and they observed a clear shift of the frequency of the break that separates the injection

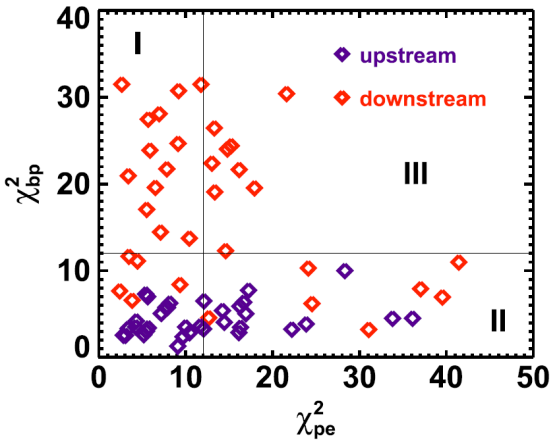

Figure 6.3: Comparison of χ^2 for "bp" and "pe" fits in upstream and downstream regions. The black thin lines show limits of good fits. Adopted from Pitňa et al. (2016).

and inertial range. They concluded that fluctuations of larger and larger scales become part of the turbulence cascade as the solar wind expands.

The other method for studying the decay of fluctuations (Bavassano et al., 1982), is to assume a stationarity of the source region and analyse the ejected plasma at various distances from the sun separated temporarily by the Sun rotational period. Bavassano et al. (1982) investigated crossings of the trailing edge of the high speed stream from HELIOS 1 and 2 mission at four heliocentric distances ($\{0.29, 0.41, 0.65, 0.87\}$AU). They analysed magnetic field power spectra within frequency range $2.8 \cdot 10^{-4} - 8.3 \cdot 10^{-2}$Hz and showed that the power within the fluctuations of the components of the magnetic field decreases with heliocentric distance as $\sim R^{-4}$ for frequencies above $\sim 2.5 \cdot 10^{-3}$. This deviation from the WKB prediction (Villante, 1980) of $\sim R^{-2.8}$ can be considered as one of the strongest evidences for the presence of the nonlinear interactions that transfer the energy stored within the large scale fluctuations down to the characteristic ion scales.

The novel approach introduced by Pitňa et al. (2017) is based on an assumption that the downstream region of an IP shock can reveal evolution of a decaying turbulence. Setting the time of the crossing of an IP shock ramp to zero, the plasma that is observed at spacecraft time t_{sp} after the shock passage was shocked at time t_{sh}. If we assume that (a) an IP shock propagates into stationary and homogenous medium and (b) expansion of the solar wind can be neglected, then a relation between these two times is

$$t_{\mathrm{sh}} = t_{\mathrm{sp}} K, \tag{6.2}$$

$$K = \frac{v_{\mathrm{sh}}}{v_{\mathrm{sh}} - \boldsymbol{v}_{\mathrm{d}} \cdot \boldsymbol{n}}, \tag{6.3}$$

where v_{sh} is the IP shock speed in the spacecraft frame of reference, $\boldsymbol{v}_{\mathrm{d}}$ is the downstream solar wind speed in the same frame and $\boldsymbol{n}$ is the shock normal. Here, we will focus on a decay of the kinetic and magnetic turbulent energy, E_{k} and E_{m} (see subsection 2.3.4). The goal is to estimate the decay law in a form

$E_\mathrm{k} \propto (t - t_{0,k})^{\alpha_\mathrm{k}}$ and $E_\mathrm{m} \propto (t - t_{0,m})^{\alpha_\mathrm{m}}$. In order to fit these phenomenological formulas to estimates of E_k and E_m from spacecraft data, one have to express the time t in proper units. These units depend on a turbulent framework under consideration (Zhou et al., 2004). For turbulence in the solar wind, the time scale associated with the transfer of energy from larger to smaller scales can be approximated by the eddy turnover time τ_nl (eq. 2.20). Using this time normalization and estimation of the kinetic and magnetic turbulent energies, it is feasible to analyze the turbulence behind IP shocks in the framework of decaying MHD turbulence.

Pitňa et al. (2017) analyzed downstream plasma measurements (10 hours) of 174 fast forward IP shocks detected at Wind spacecraft. The kinetic and magnetic energies were estimated as

$$E_\mathrm{k} = \frac{1}{2}\langle\rho\rangle_{\delta t} \sum_{i=0}^{2} var_{\delta t}(v_i) \tag{6.4}$$

and

$$E_\mathrm{m} = \frac{1}{2\mu_0} \sum_{i=0}^{2} var_{\delta t}(B_i), \tag{6.5}$$

where $\langle\rangle_{\delta t}$ and $var_{\delta t}$ denotes the mean and variance of a quantity on a timescale $\delta t = 30$ min (in the spacecraft frame of reference). The first sample starts 2 minutes after the shock ramp and each next one is shifted by 5 minutes. Moreover, the spacecraft time, t_nl is expressed in units of the eddy turnover time via

$$t_\mathrm{nl} = \frac{t_\mathrm{sp} K}{\tau_\mathrm{nl}}, \tag{6.6}$$

where τ_nl is estimated as

$$\tau_\mathrm{nl} = \frac{\langle|v_\mathrm{d}|\rangle_{\delta t}\, \delta t}{2\pi\sqrt{\sum_{i=0}^{2} var_{\delta t}(v_{\mathrm{d},i})}}. \tag{6.7}$$

Figure 6.4 shows the downstream energy profiles of E_k and E_m after each shock (upper and lower plots differ in the scales of the axes only). Profiles are normalized by their immediate downstream values. The red crosses and blue diamonds show the geometric averages of the profiles in logarithmically scaled time bins. The corresponding red and blue lines show fits of a phenomenological power law,

$$E(t_\mathrm{nl}) = \left(\frac{t_\mathrm{nl} - t_0}{t_\mathrm{d} - t_0}\right)^{\alpha}, \tag{6.8}$$

where t_d reflects the fact that the decay starts at $t_\mathrm{nl} \approx 10$ as it is clearly seen in the figure. Pitňa et al. (2017) reported the parameters of the decay with a model function (eq. 6.8) for the kinetic energy, $t_{0,\mathrm{k}} = 0 \pm 2$ and $\alpha_\mathrm{k} = -1.2 \pm 0.1$ and for the magnetic energy, $t_{0,\mathrm{m}} = -4 \pm 2$ and $\alpha_\mathrm{m} = -1.2 \pm 0.1$. These asymptotic exponents are in agreement with both theoretically derived (Biskamp, 2003) and MHD simulation (Biskamp and Müller, 2000) values. However, the parameter t_d was not previously reported. Pitňa et al. (2017) suggested that this additional time constant is connected with the kinetic physics immediately downstream of an IP shock. On the basis of measurements of one IP shock, they hypothesised

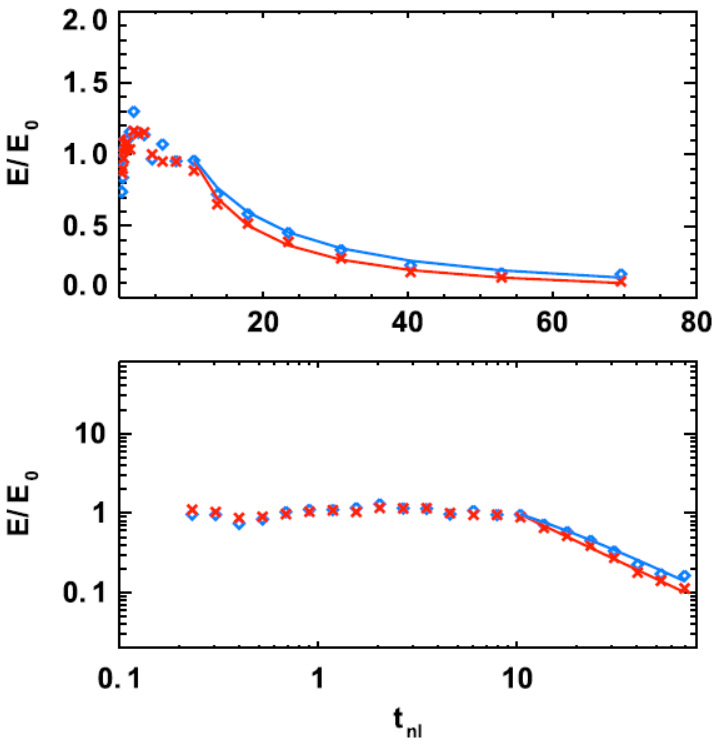

Figure 6.4: Normalized kinetic (red crosses) and magnetic (blue circles) energy profiles. The values are displayed in a linear scale (upper panel) and a log–log scale (bottom panel). The red and blue curves denote the best power-law model functions from the nonlinear least squares analysis. E/E_0 on the y-axis denotes either $E_\mathrm{k}/E_{\mathrm{k},0}$ or $E_\mathrm{b}/R_{\mathrm{b},0}$. Adopted from Pitňa et al. (2017).

that the processes which lead to inhibition of the turbulent cascade immediately downstream of an IP shock could be treated as an inverse turbulent cascade (Christensson et al., 2001). However, further investigations are needed to test this hypothesis.

6.3 Nature of kinetic fluctuations

In this section, we focus on turbulent fluctuations within the pristine solar wind whose spatial dimensions are comparable to or smaller than the characteristic proton scales, i.e, its thermal gyroradius and/or inertial length (see eqs. 1.2 and 1.3, respectively). We exclude solar wind intervals close to the IP or bow shock ramps that are frequently spoiled by wave like structures caused by the kinetic processes close the shock ramp (i.e., particle reflections, various wave-particle instabilities, etc.). We are interested in more or less stationary turbulent system that is free of major large-scale energy sources and we analyze the kinetic range fluctuations within such freely decaying turbulence.

As it was shown by many authors (Bale et al., 2005; Chen et al., 2013; Podesta, 2013), the fluctuations around ρ_gp exhibit characteristics of a linear KAW mode (see chapters 2.1.2 and 2.3.3). Chen et al. (2013) proposed a new method to distinguish whether the fluctuations are in whistler or KAW modes. Based on both numerical simulation of the nonlinear kinetic Alfvén equations and statistics of

17 intervals, they concluded that turbulence at sub-proton scales is mostly KAW in nature. Grošelj et al. (2018) extended the method of Chen et al. (2013) and showed that both wave like and more intermittent fluctuations follow the linear features of KAWs. Recently, Wu et al. (2019) and Roberts et al. (2018) showed that sub-ion scales within Earth's magnetosheath turbulence are populated by fluctuations that fit the linear KAW relations. Due to the lack of high-cadence plasma measurements, such a comprehensive study within the pristine solar wind is still missing. Although the studies mentioned above are highly valuable, they are either case studies or their sample size is small. On the other hand, Pitňa et al. (2019) attempted to address the question of how typical is the presence of KAW like fluctuations within the kinetic range of turbulence. By a combination of measurements from two spacecraft (Wind and Spektr-R), they were able to cover a wide range of solar wind conditions with statistically sound 465 cases.

Since the study combines two data sets from different spacecraft which are separated by $\sim 150 - 250\ R_{\mathrm{E}}$, the question of applicability of such an approach arises. However, Šafránková et al. (2019) demonstrated that a mean value of the magnetic field vector measured at Wind can be applied at Spektr-R locations. Moreover, they show that the inertial range fluctuations of the solar wind velocity at both locations are similar. A propagation procedure that identifies the same or similar solar wind plasma at both spacecraft can be briefly summarized as it follows: (a) lets denote a desired interval at Spektr-R as $(t_1 - t_2)_{\mathrm{S}}$, (b) a corresponding interval at Wind, $(t_1 - t_2)_{\mathrm{W}}$ is computed as

$$(t_1 - t_2)_{\mathrm{W}} = (t_1 - t_2)_{\mathrm{S}} - \Delta t, \tag{6.9}$$

where $\Delta t = \Delta R / \langle V_{\mathrm{sw}} \rangle$, ΔR is the separation between the spacecraft along the solar wind flow, and $\langle V_{\mathrm{sw}} \rangle$ is the average solar wind speed computed from the Spektr-R (BMSW) measurements within the desired time range. For more detailed description and the selection of intervals for further data processing see the attached paper (A5).

We adapt the technique of Chen et al. (2013) and generalize it as it follows. Assuming that we have high-cadence measurements of at least two independent quantities (i.e., density and magnitude of the magnetic field), then (a) we estimate a certain ratio of the average fluctuations of these quantities at the scale of interest; (b) we find a theoretical prescription of this ratio for a specific wave mode (i.e., KAW, whisler, ion-Bernstein), and finally, (c) we take a ratio Q between the observed and theoretical values of this ratio. On the basis of the Q value, we can discriminate between the wave modes.

Pitňa et al. (2019) analyzed the following three non-dimensional ratios: the ratio of normalized density and perpendicular magnetic field fluctuations,

$$R_{nB_\perp} \equiv \frac{(\delta N / N_0)^2}{(\delta B_\perp / B_0)^2}, \tag{6.10}$$

magnetic compressibility,

$$C_\parallel \equiv \frac{\delta B_\parallel^2}{\delta B^2}, \tag{6.11}$$

and

$$R_{nV} \equiv \frac{(\delta N/N_0)^2}{(\delta V_{\rm sw}/V_{\rm A})^2}, \tag{6.12}$$

where, δN, δB, $\delta B_\perp$, $\delta B_\parallel$ and $\delta V_{\rm sw}$ denote the density, magnetic field strength, perpendicular magnetic field, parallel magnetic field and velocity fluctuations. Let us designate the set $R \equiv \{R_{nB_\perp}, C_\parallel, R_{nV}\}$. For each of the analyzed interval within the statistics, Pitňa et al. (2019) calculated both experimentally estimated values of R, denoted as $R^{\rm obs} \equiv \{R^{\rm obs}_{nB_\perp}, C^{\rm obs}_\parallel, R^{\rm obs}_{nV}\}$, and expected values for KAWs in the framework of the two-fluid MHD (Zhao et al., 2014) and/or kinetic Vlasov-Maxwell equations (Boldyrev et al., 2013), denoted as $R^{\rm th} \equiv \{R^{\rm th}_{nB_\perp}, C^{\rm th}_\parallel, R^{\rm th}_{nV}\}$ (see eqs. (1–8) of Pitňa et al. (2019)). Finally, the ratio of observed and theoretical values was calculated as

$$Q^{\rm KAW} \equiv \{R^{\rm obs}_{nB_\perp}/R^{\rm th}_{nB_\perp}, C^{\rm obs}_\parallel/C^{\rm th}_\parallel, R^{\rm obs}_{nV}/R^{\rm th}_{nV}\} \equiv \{R_{\rm KAW}, C_{\rm KAW}, A_{\rm KAW}\}. \tag{6.13}$$

In the estimation of $R^{\rm obs}$, the PSDs of magnetic field components and magnitude (from Wind, MFI), ion density and solar wind velocity (from Spektr-R, BMSW) were used as a proxy for δN, δB, $\delta B_\perp$, $\delta B_\parallel$ and $\delta V_{\rm sw}$ in eqs. 6.10, 6.11 and 6.12. The PSDs were estimated via Continuous Wavelet Transform (CWT). Therefore, the ratios $Q^{\rm KAW}$ are scale dependent, i.e., $Q^{\rm KAW} = Q^{\rm KAW}(k\rho_{\rm gp})$, where the scale is expressed in the units of the proton gyroradii. Figure 6.5 shows the profiles of $Q_{\rm KAW}(k\rho_{\rm gp})$ for all analyzed intervals in Pitňa et al. (2019). Each panel of the figure clearly shows that the scale at which the ratio Q is close to unity, i.e., that the fluctuations follow the KAW relations, is the spatial scale of the proton gyroradius, $k\rho_{\rm gp} \approx 1$. Note that the decrease of $R_{\rm KAW}$ of the median curve (solid red) for $k\rho_{\rm gp} \gtrapprox 2$ is caused by a noise in the magnetic field measurements. For a more comprehensive description of the figure, see Pitňa et al. (2019).

Pitňa et al. (2019) reported the median values of $Q_{\rm KAW}$ at $k\rho_{\rm gp} = 2$: $R_{\rm KAW} \approx 0.7$, $C_{\rm KAW} \approx 0.9$ and $A_{\rm KAW} \approx 1.2$. These values suggest that the kinetic range fluctuations roughly follow the KAW relations on average. However, the spread of the profiles around these median values is significant. Such spread is often attributed to the noise (error) of observations and thus Pitňa et al. (2019) decided to assess the contribution of the measurement error in the observed profiles.

The errors can be separated into two categories, (1) the errors that come from either the uncertainty of measurements and/or the inherent fluctuations of analyzed quantities and (2) the errors that arise from the propagation procedure. Considering the former, the authors focus on two characteristics of a Probability Distribution Function (PDF) of $Q^{\rm KAW}$ at $k\rho_{\rm gp} = 2$, namely, variance of PDF and a so-called Confidence Interval Factor (CIF). While the definition of variance is obvious, CIF is defined as a ratio of the upper and lower bound of the central confidence interval $[c_{\rm l}, c_{\rm u}]$, with the following condition $\int_{c_{\rm l}}^{c_{\rm u}} PDF(x){\rm d}x = 0.68$. The variances and CIFs for the PDFs of $Q^{\rm KAW}$ are depicted as colored vertical lines in Figure 6.6a and 6.6b, respectively. To assess the contribution of the error measurements, Pitňa et al. (2019) estimated variances and CIFs of the error distribution functions of $R_{\rm KAW}$, $C_{\rm KAW}$ and $A_{\rm KAW}$ for each analyzed interval (465 cases). In approximation of the error PDF, they employed a Monte Carlo (MC) simulations technique. For details of computation see Pitňa et al. (2019). The results of the simulation are shown as histograms of variances and CIFs of

error PDFs in Figure 6.6. For both quantities, the majority $\approx 80 - 90\%$ of the values obtained from simulations are lower than the variances and CIFs of the original PDFs whereas this percentage should be close to $\approx 50\%$ if the errors of measurements would be significant.

Furthermore, Pitňa et al. (2019) argued that the errors introduced by the propagation of solar wind is also small. The key point of the argument lied in the comparison of the distribution of R_{KAW} obtained by Chen et al. (2013) and their distribution. They argued that both PDFs cover the same range of values $R_{\mathrm{KAW}} \in [\approx 0.1, \approx 5]$, thus, the propagation error should be small.

In conclusion, Pitňa et al. (2019) found that the fluctuations of solar wind plasma around the scales of thermal gyroradius of the proton follow the relations for the kinetic Alfvén wave mode. However, the significant spread of *observed/predicted* ratios cannot be explained only by the measurement errors. The reasons for the deviations could be manifold–the presence of other wave modes in the kinetic range, temperature anisotropy, coherent structures, etc. and the authors plan to address a few of these factors in following studies.

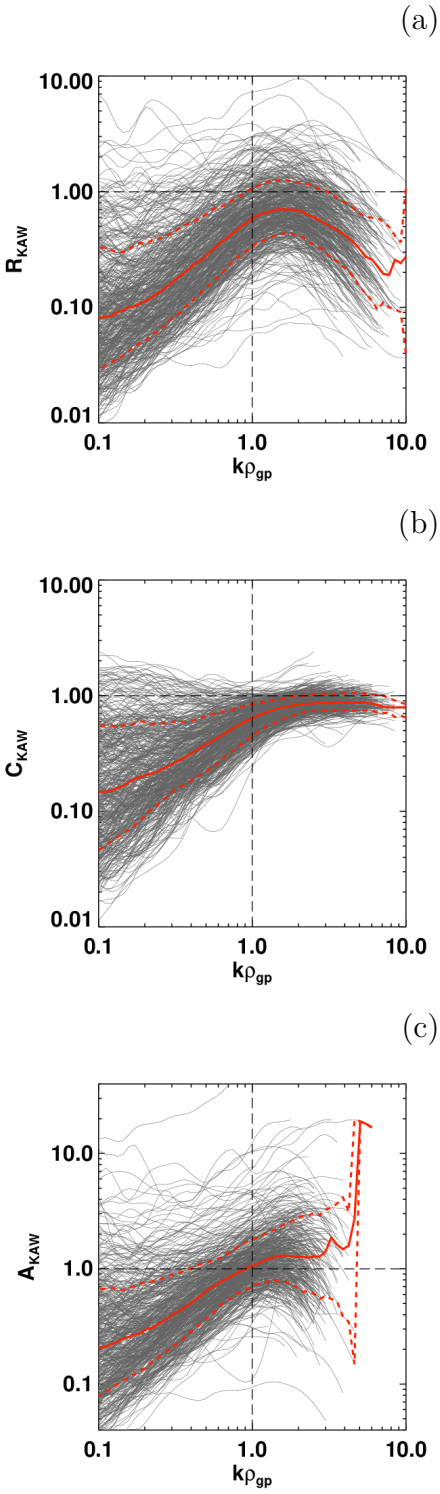

Figure 6.5: (a) R_{KAW}, (b) C_{KAW}, (c) A_{KAW} as a function of $k\rho_{\mathrm{gp}}$. The solid red curve denotes the median value of the whole set. Dashed red lines mark the central confidence interval that contains 68% of values at a given scale. Adopted from Pitňa et al. (2019)

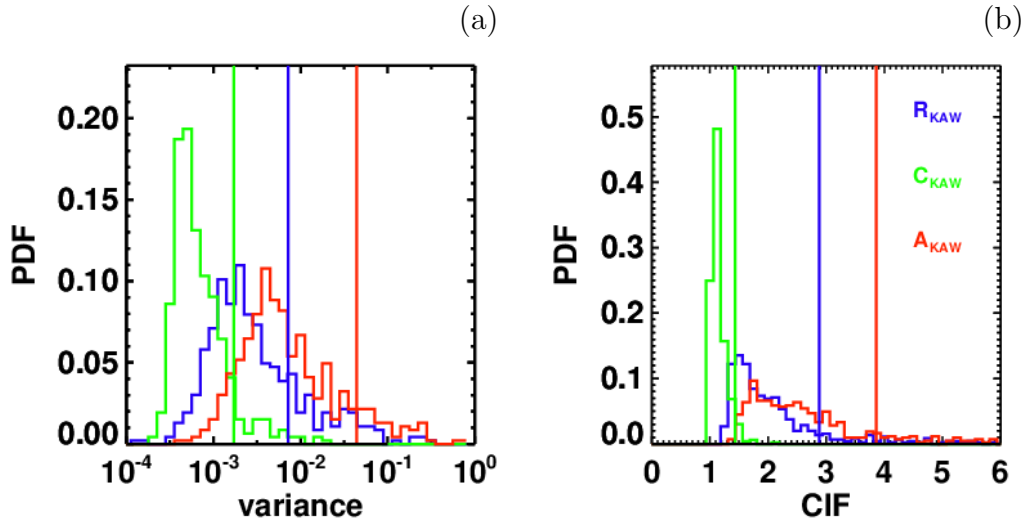

Figure 6.6: Results of MC simulations of uncertainties of R_{KAW} (green), C_{KAW} (blue), and A_{KAW} (red) at $k\rho_{\mathrm{gp}} = 2$. (a) The PDF's of the variances. Each simulation has 10^5 runs for each interval and each quantity. (b) The PDF's of the CIFs. The colored vertical lines mark the variances and CIFs estimated from the original set. Adopted from Pitňa et al. (2019)

Chapter 7

Conclusion

The complex nature of plasma flows with high Reynolds numbers attracts attention due to the presence of this state of matter throughout the universe. Turbulence, especially its magnetohydrodynamic extension, is not fully understood even when we account for the recent progress. For example, the exact mechanism that ultimately heat the solar wind are unresolved. New knowledge would come from computer simulations of this complex system and from high cadence *in situ* measurements (Spektr-R, MMS, Solar Orbiter, Parker Solar Probe, etc.). In the present thesis, we analyzed unique BMSW measurements with the sampling frequency of 32 Hz that allowed us to addressed afew issues concerning the complex shape of the turbulent power spectrum and its decay. We can summarize our results as:

1. Under assumption that the power spectrum of the density fluctuations upstream of fast forward IP shocks can be well approximated by three power law segments in the frequency range from 0.001 to 8 Hz, the IP shock induces the following changes: (a) The power within the inertial range fluctuations increases tenfold on average but the properties of the turbulent cascade are conserved across the shock; (b) The spectra in the kinetic range, i.e., for frequencies higher than the high-frequency break associated with f_{gp} (spacecraft frame frequency of ρ_{gp}), are steeper that their upstream counterparts, whereas (c) in approximately half of the cases, the spectra exhibit a curvature and can be better described as an exponentially truncated power law (Pitňa et al., 2016). Observation connected with (c) suggest that turbulent cascade may not be applicable in the kinetic range.

2. The decay of inertial range fluctuations behind an IP shock follows a power law behaviour $E \propto t^{\alpha}$, $\alpha \approx -1.2$ for large times and this is true for both kinetic and magnetic energy. The exponent $\alpha_{\mathrm{k}} \approx \alpha_{\mathrm{m}} \approx -1.2$, is characteristic for the turbulent system with vanishing magnetic helicity (Biskamp and Müller, 2000; Biskamp, 2003). Pitňa et al. (2019) observed a slight dominance of the magnetic energy over kinetic energy in the later stages of the decay, which is consistent with the fact that the solar wind exhibits non-zero magnetic helicity (Matthaeus and Goldstein, 1982).

3. Pitňa et al. (2017) found that the decay does not start immediately after the passage of an IP shock, but at time $t = t_{\mathrm{d}} = 10$, where t is measured in the units of eddy turnover time. This constant is the same for the decay of

both magnetic and kinetic energies. Pitňa et al. (2017) suggested that this constant can be attributed to the kinetic processes originating at the shock ramp.

4. Considering the nature of kinetic range fluctuations, Pitňa et al. (2019) have convincingly shown that KAW mode plays a crucial role in the dynamics of solar wind turbulence around ion characteristic scales. They found KAW as a dominant mode for a broad range of solar wind conditions. They also reported some deviations from KAW predictions and discussed a role of the measurement errors. Their findings are supported by other studies on kinetic range turbulence that analyze either the scarce high cadence measurements of MMS and THEMIS (Roberts et al., 2018; Wu et al., 2019; Chen et al., 2013), and/or simulation studies (Franci et al., 2015, 2018; Grošelj et al., 2018).

As a conclusion, we would like to remark that high-cadence measurements of the BMSW instrument provide an unique insight into the kinetic range of plasma turbulence. The goals of the thesis have been fulfilled but they also open new questions. Namely, further investigations of the nature of the turbulence in the kinetic range would address the deviations from the KAW predictions.

Bibliography

O. Alexandrova, V. Carbone, P. Veltri, and L. Sorriso-Valvo. Small-Scale Energy Cascade of the Solar Wind Turbulence. *Astrophysical Journal*, 674:1153–1157, Feb 2008.

O. Alexandrova, J. Saur, C. Lacombe, A. Mangeney, J. Mitchell, S. J. Schwartz, and P. Robert. Universality of Solar-Wind Turbulent Spectrum from MHD to Electron Scales. *Physical Review Letters*, 103(16):165003, Oct 2009.

O. Alexandrova, C. Lacombe, A. Mangeney, R. Grappin, and M. Maksimovic. Solar Wind Turbulent Spectrum at Plasma Kinetic Scales. *Astrophysical Journal*, 760(2):121, Dec 2012.

H. Alfvén. Interplanetary Magnetic Field. In B. Lehnert, editor, *Electromagnetic Phenomena in Cosmical Physics*, volume 6 of *IAU Symposium*, page 284, Jan 1958.

H. W. Babcock. The Topology of the Sun's Magnetic Field and the 22-YEAR Cycle. *Astrophysical Journal*, 133:572, Mar 1961.

S. D. Bale, P. J. Kellogg, F. S. Mozer, T. S. Horbury, and H. Reme. Measurement of the Electric Fluctuation Spectrum of Magnetohydrodynamic Turbulence. *Physical Review Letters*, 94(21):215002, Jun 2005.

A. Balogh and R. A. Treumann. *Physics of Collisionless Shocks*. Springer-Verlag New York, First Edition edition, 2013.

A. Barnes. *Hydromagnetic waves and turbulence in the solar wind*. 1979.

G. K. Batchelor. *The Theory of Homogeneous Turbulence*. Cambridge University Press, Cambridge, UK, 1982. ISBN 0521041171.

B. Bavassano, M. Dobrowolny, F. Mariani, and N. F. Ness. Radial evolution of power spectra of interplanetary Alfvenic turbulence. *Journal of Geophysical Research*, 87:3617–3622, May 1982.

L. Biermann. Kometenschweife und solare Korpuskularstrahlung. *Zeitschrift f ur Astrophysik*, 29:274, 1951.

D. Biskamp. *Magnetohydrodynamic Turbulence*. Cambridge University Press, 2003.

D. Biskamp and W. C. Müller. Decay Laws for Three-Dimensional Magnetohydrodynamic Turbulence. *Physical Review Letters*, 83(11):2195–2198, Sep 1999.

D. Biskamp and W. C. Müller. Scaling properties of three-dimensional isotropic magnetohydrodynamic turbulence. *Physics of Plasmas*, 7:4889–4900, Dec 2000.

S. Boldyrev and J. C. Perez. Spectrum of Kinetic-Alfvén Turbulence. *The Astrophysical Journal Letters*, 758:L44, Oct 2012.

S. Boldyrev, K. Horaites, Q. Xia, and J. C. Perez. Toward a Theory of Astrophysical Plasma Turbulence at Subproton Scales. *Astrophysical Journal*, 777 (1):41, Nov 2013.

R. Bruno and V. Carbone. The Solar Wind as a Turbulence Laboratory. *Living Reviews in Solar Physics*, 10:2, May 2013.

R. Bruno, V. Carbone, Z. Vörös, R. D'Amicis, B. Bavassano, M. B. Cattaneo, A. Mura, A. Milillo, S. Orsini, P. Veltri, L. Sorriso-Valvo, T. Zhang, H. Biernat, H. Rucker, W. Baumjohann, D. Jankovičová, and P. Kovács. Coordinated Study on Solar Wind Turbulence During the Venus-Express, ACE and Ulysses Alignment of August 2007. *Earth Moon and Planets*, 104:101–104, Apr 2009.

R. C. Carrington. Description of a Singular Appearance seen in the Sun on September 1, 1859. *Monthly Notices of the Royal Astronomical Society*, 20: 13–15, Nov 1859.

B. D. G. Chandran, E. Quataert, G. G. Howes, Q. Xia, and P. Pongkitiwanichakul. Constraining Low-Frequency Alfvénic Turbulence in the Solar Wind Using Density-Fluctuation Measurements. *Astrophysical Journal*, 707: 1668–1675, Dec 2009.

C. H. K. Chen. Recent progress in astrophysical plasma turbulence from solar wind observations. *Journal of Plasma Physics*, 82(6):535820602, Dec 2016.

C. H. K. Chen, R. T. Wicks, T. S. Horbury, and A. A. Schekochihin. Interpreting power anisotropy measurements in plasma turbulence. *Astrophysical Journal Letters*, 711(2):L79, 2010.

C. H. K. Chen, A. Mallet, T. A. Yousef, A. A. Schekochihin, and T. S. Horbury. Anisotropy of Alfvénic turbulence in the solar wind and numerical simulations. *Monthly Notices of the Royal Astronomical Society*, 415(4):3219–3226, Aug 2011.

C. H. K. Chen, S. Boldyrev, Q. Xia, and J. C. Perez. Nature of Subproton Scale Turbulence in the Solar Wind. *Physical Review Letters*, 110(22):225002, May 2013.

C. H. K. Chen, L. Leung, S. Boldyrev, B. A. Maruca, and S. D. Bale. Ion-scale spectral break of solar wind turbulence at high and low beta. *Geophysical Research Letters*, 41(22):8081–8088, Nov 2014a.

C. H. K. Chen, L. Leung, S. Boldyrev, B. A. Maruca, and S. D. Bale. Ion-scale spectral break of solar wind turbulence at high and low beta. *Geophysical Research Letters*, 41(22):8081–8088, Nov 2014b.

F. F. Chen. *Introduction to Plasma Physics*. Springer US, New York, 1974. ISBN 978-1-4757-0461-7.

G. F. Chew, M. L. Goldberger, and F. E. Low. The boltzmann equation and the one-fluid hydromagnetic equations in the absence of particle collisions. *Proceedings of the Royal Society of London. Series A. Mathematical and Physical Sciences*, 236(1204):112–118, 1956.

J. Cho and E. T. Vishniac. The Anisotropy of Magnetohydrodynamic Alfvénic Turbulence. *Astrophysical Journal*, 539(1):273–282, Aug 2000.

M. Christensson, M. Hindmarsh, and A. Brandenburg. Inverse cascade in decaying three-dimensional magnetohydrodynamic turbulence. *Physical Review E*, 64:056405, Oct 2001.

P. J. Coleman, Jr. Turbulence, Viscosity, and Dissipation in the Solar-Wind Plasma. *Astrophysical Journal*, 153:371, Aug 1968.

R. D'Amicis, R. Bruno, G. Pallocchia, B. Bavassano, D. Telloni, V. Carbone, and A. Balogh. Radial Evolution of Solar Wind Turbulence during Earth and Ulysses Alignment of 2007 August. *Astrophysical Journal*, 717(1):474–480, Jul 2010.

S. Danilovic, M. Schüssler, and S. K. Solanki. Probing quiet Sun magnetism using MURaM simulations and Hinode/SP results: support for a local dynamo. *Astronomy and Astrophysics*, 513:A1, Apr 2010.

P. A. Davidson. *Turbulence - An Introduction for Scientists and Engineers*. Oxford University Press, New York, 2004. ISBN 019852948.

P. A. Davidson, Y. Kaneda, K. Moffatt, and K. R. Sreenivasan. *A Voyage Through Turbulence*. Cambridge University Press, Cambridge, 2011.

T. de Karman and L. Howarth. On the Statistical Theory of Isotropic Turbulence. *Proceedings of the Royal Society of London Series A*, 164(917):192–215, Jan 1938.

L. Del Zanna. Parametric decay of oblique arc-polarized Alfvén waves. *Geophysical Research Letters*, 28(13):2585–2588, Jan 2001.

L. Del Zanna, L. Matteini, S. Landi, A. Verdini, and M. Velli. Parametric decay of parallel and oblique Alfvén waves in the expanding solar wind. *Journal of Plasma Physics*, 81(1):325810102, Jan 2015.

N. F. Derby, Jr. Modulational instability of finite-amplitude, circularly polarized Alfven waves. *Astrophysical Journal*, 224:1013–1016, Sep 1978.

A. Dosch and A. Shalchi. Diffusive shock acceleration at interplanetary perpendicular shock waves: Influence of the large scale structure of turbulence on the maximum particle energy. *Advances in Space Research*, 46(9):1208–1217, Nov 2010.

T. Dudok de Wit, O. Alexandrova, I. Furno, L. Sorriso-Valvo, and G. Zimbardo. Methods for Characterising Microphysical Processes in Plasmas. *Space Science Reviews*, 178(2-4):665–693, Oct 2013.

G. Falkovich and K. R. Sreenivasan. Lessons from hydrodynamic turbulence. *Physics Today*, 59(4):43–49, 2006.

L. A. Fisk, N. A. Schwadron, and T. H. Zurbuchen. Acceleration of the fast solar wind by the emergence of new magnetic flux. *Journal of Geophysical Research*, 104(A9):19765–19772, Sep 1999.

L. Franci, S. Landi, L. Matteini, A. Verdini, and P. Hellinger. High-resolution Hybrid Simulations of Kinetic Plasma Turbulence at Proton Scales. *Astrophysical Journal*, 812:21, Oct 2015.

L. Franci, S. Landi, A. Verdini, L. Matteini, and P. Hellinger. Solar Wind Turbulent Cascade from MHD to Sub-ion Scales: Large-size 3D Hybrid Particle-in-cell Simulations. *Astrophysical Journal*, 853:26, Jan 2018.

P. Frick and R. Stepanov. Long-term free decay of MHD turbulence. *Europhysics Letters*, 92(3):34007, Nov 2010.

U. Frisch, A. Pouquet, J. Léorat, and A. Mazure. Possibility of an inverse cascade of magnetic helicity in magnetohydrodynamic turbulence. *Journal of Fluid Mechanics*, 68(4):769–778, 1975.

X. Fu, H. Li, F. Guo, X. Li, and V. Roytershteyn. Parametric Decay Instability and Dissipation of Low-frequency Alfvén Waves in Low-beta Turbulent Plasmas. *Astrophysical Journal*, 855(2):139, Mar 2018.

G. A. Gary. Plasma Beta above a Solar Active Region: Rethinking the Paradigm. *Solar Physics*, 203:71–86, Oct 2001.

S. P. Gary. *Theory of Space Plasma Microinstabilities*. Cambridge, UK: Cambridge University Press, Cambridge, 1993. ISBN 0521431670.

P. R. Gazis, A. Barnes, J. D. Mihalov, and A. J. Lazarus. Solar wind velocity and temperature in the outer heliosphere. *Journal of Geophysical Research*, 99: 6561–6573, Apr 1994.

P. Goldreich and S. Sridhar. Toward a theory of interstellar turbulence. 2: Strong alfvenic turbulence. *Astrophysical Journal*, 438:763–775, Jan 1995.

M. L. Goldstein. An instability of finite amplitude circularly polarized Alfven waves. *Astrophysical Journal*, 219:700–704, Jan 1978.

O. Goncharov, J. Šafránková, Z. Němeček, L. Přech, A. Pitňa, and G. N. Zastenker. Upstream and downstream wave packets associated with low-Mach number interplanetary shocks. *Geophysical Research Letters*, 41(22):8100–8106, Nov 2014.

R. Grappin, M. Velli, and A. Mangeney. 'Alfvenic' versus 'standard' turbulence in the solar wind. *Annales Geophysicae*, 9:416–426, Jun 1991.

D. Grošelj, A. Mallet, N. F. Loureiro, and F. Jenko. Fully Kinetic Simulation of 3D Kinetic Alfvén Turbulence. *Physical Review Letters*, 120(10):105101, Mar 2018.

T. Hatori. Kolmogorov-style argument for the decaying homogeneous mhd turbulence. *Journal of the Physical Society of Japan*, 53(8):2539–2545, 1984.

P. Hellinger, P. Trávníček, J. C. Kasper, and A. J. Lazarus. Solar wind proton temperature anisotropy: Linear theory and WIND/SWE observations. *Geophysical Research Letters*, 33(9):L09101, May 2006.

R. Hodgson. On a curious Appearance seen in the Sun. *Monthly Notices of the Royal Astronomical Society*, 20:15–16, Nov 1859.

J. V. Hollweg. Alfvén waves in the solar wind: Wave pressure, poynting flux, and angular momentum. *Journal of Geophysical Research*, 78(19):3643, Jan 1973.

J. V. Hollweg. Beat, modulational, and decay instabilities of a circularly polarized Alfvén wave. *Journal of Geophysical Research*, 99(A12):23431–23448, Dec 1994.

J. V. Hollweg. Kinetic Alfvén wave revisited. *Journal of Geophysical Research*, 104:14811–14820, Jul 1999.

T. S. Horbury. Waves and Turbulence in the Solar Wind – an Overview. In Michał Ostrowski and Reinhard Schlickeiser, editors, *Plasma Turbulence and Energetic Particles in Astrophysics*, pages 115–134, Dec 1999.

T. S. Horbury, M. Forman, and S. Oughton. Anisotropic Scaling of Magnetohydrodynamic Turbulence. *Physical Review Letters*, 101(17):175005, Oct 2008.

T. S. Horbury, R. T. Wicks, and C. H. K. Chen. Anisotropy in Space Plasma Turbulence: Solar Wind Observations. *Space Science Reviews*, 172(1-4):325–342, Nov 2012.

M. Hossain, P. C. Gray, D. H. Pontius Jr., W. H. Matthaeus, and S. Oughton. Phenomenology for the decay of energy-containing eddies in homogeneous mhd turbulence. *Physics of Fluids*, 7(11):2886–2904, 1995.

G. G. Howes, S. C. Cowley, W. Dorland, G. W. Hammett, E. Quataert, and A. A. Schekochihin. Astrophysical Gyrokinetics: Basic Equations and Linear Theory. *Astrophysical Journal*, 651:590–614, Nov 2006.

G. G. Howes, J. M. Tenbarge, W. Dorland, E. Quataert, A. A. Schekochihin, R. Numata, and T. Tatsuno. Gyrokinetic Simulations of Solar Wind Turbulence from Ion to Electron Scales. *Physical Review Letters*, 107(3):035004, Jul 2011.

G. G. Howes, S. D. Bale, K. G. Klein, C. H. K. Chen, C. S. Salem, and J. M. TenBarge. The Slow-mode Nature of Compressible Wave Power in Solar Wind Turbulence. *Astrophysical Journal*, 753(1):L19, Jul 2012.

P. S. Iroshnikov. Turbulence of a Conducting Fluid in a Strong Magnetic Field. *Sov. Astron.*, 40:742, 1963.

D. B. Jess, M. Mathioudakis, R. Erdélyi, P. J. Crockett, F. P. Keenan, and D. J. Christian. Alfvén waves in the lower solar atmosphere. *Science*, 323(5921): 1582–1585, 2009.

J. R. Jokipii and Joseph V. Hollweg. Interplanetary Scintillations and the Structure of Solar-Wind Fluctuations. *Astrophysical Journal*, 160:745, May 1970.

J. C. Kasper, A. J. Lazarus, J. T. Steinberg, K. W. Ogilvie, and A. Szabo. Physics-based tests to identify the accuracy of solar wind ion measurements: A case study with the Wind Faraday Cups. *Journal of Geophysical Research (Space Physics)*, 111(A3):A03105, Mar 2006.

K. G. Klein, G. G. Howes, J. M. TenBarge, S. D. Bale, C. H. K. Chen, and C. S. Salem. Using Synthetic Spacecraft Data to Interpret Compressible Fluctuations in Solar Wind Turbulence. *Astrophysical Journal*, 755(2):159, Aug 2012.

A. Kolmogorov. The Local Structure of Turbulence in Incompressible Viscous Fluid for Very Large Reynolds' Numbers. *Akademiia Nauk SSSR Doklady*, 30: 301–305, 1941.

R. H. Kraichnan. Inertial Range Spectrum of Hydromagnetic Turbulence. *Physics of Fluids*, 8:1385–1387, 1965.

R. H. Kraichnan. Helical turbulence and absolute equilibrium. *Journal of Fluid Mechanics*, 59(4):745–752, 1973.

P. O. K. Krehl. *History of Shock Waves, Explosions and Impact*. First Edition. Springer-Verlag, Berlin Heidelberg, 2007. ISBN 978-3-540-20678-1.

R. J. Leamon, C. W. Smith, N. F. Ness, W. H. Matthaeus, and H. K. Wong. Observational constraints on the dynamics of the interplanetary magnetic field dissipation range. *Journal of Geophysical Research*, 103:4775, Mar 1998.

R. P. Lepping, M. H. Acũna, L. F. Burlaga, W. M. Farrell, J. A. Slavin, K. H. Schatten, F. Mariani, N. F. Ness, F. M. Neubauer, and Y. C. Whang. The Wind Magnetic Field Investigation. *Space Science Reviews*, 71(1-4):207–229, Feb 1995.

Q. Lu, Q. Hu, and G. P. Zank. The Interaction of Alfvén Waves with Perpendicular Shocks. *Astrophysical Journal*, 706(1):687–692, Nov 2009.

A. H. Luttrell and A. K. Richter. A study of MHD fluctuations upstream and downstream of quasi-parallel interplanetary shocks. *Journal of Geophysical Research*, 92(A3):2243–2252, Mar 1987.

E. Marsch. Kinetic Physics of the Solar Corona and Solar Wind. *Living Reviews in Solar Physics*, 3, Jul 2006.

E. Marsch. Solar wind and kinetic heliophysics. *Annales Geophysicae*, 36(6): 1607–1630, 2018.

E. Marsch and C. Y. Tu. Spectral and spatial evolution of compressible turbulence in the inner solar wind. *Journal of Geophysical Research*, 95(A8):11945–11956, Aug 1990.

L. Matteini, S. Landi, L. Del Zanna, M. Velli, and P. Hellinger. Parametric decay of linearly polarized shear Alfvén waves in oblique propagation: One and two-dimensional hybrid simulations. *Geophysical Research Letters*, 37(20):L20101, Oct 2010.

L. Matteini, D. Stansby, T. S. Horbury, and C. H. K. Chen. On the 1/f Spectrum in the Solar Wind and Its Connection with Magnetic Compressibility. *Astrophysical Journal*, 869(2):L32, Dec 2018.

W. H. Matthaeus and M. L. Goldstein. Measurement of the rugged invariants of magnetohydrodynamic turbulence in the solar wind. *Journal of Geophysical Research*, 87(A8):6011–6028, Aug 1982.

W. H. Matthaeus and M. Velli. Who Needs Turbulence?. A Review of Turbulence Effects in the Heliosphere and on the Fundamental Process of Reconnection. *Space Science Reviews*, 160(1-4):145–168, Oct 2011.

W. H. Matthaeus, M. L. Goldstein, and J. H. King. An interplanetary magnetic field ensemble at 1 AU. *Journal of Geophysical Research*, 91(A1):59–69, Jan 1986.

W. H. Matthaeus, S. Dasso, J. M. Weygand, L. J. Milano, C. W. Smith, and M. G. Kivelson. Spatial Correlation of Solar-Wind Turbulence from Two-Point Measurements. *Physical Review Letters*, 95(23):231101, Dec 2005.

W. H. Matthaeus, A. Pouquet, P. D. Mininni, P. Dmitruk, and B. Breech. Rapid Alignment of Velocity and Magnetic Field in Magnetohydrodynamic Turbulence. *Physical Review Letters*, 100(8):085003, Feb 2008.

W. H. Matthaeus, D. C. Montgomery, M. Wan, and S. Servidio. A review of relaxation and structure in some turbulent plasmas: magnetohydrodynamics and related models. *Journal of Turbulence*, 13:N37, 2012.

D. J. McComas, B. L. Barraclough, J. T. Gosling, C. M. Hammond, J. L. Phillips, M. Neugebauer, A. Balogh, and R. J. Forsyth. Structures in the polar solar wind: Plasma and field observations from Ulysses. *Journal of Geophysical Research*, 100(A10):19893–19902, Oct 1995.

D. Montgomery and L. Turner. Anisotropic magnetohydrodynamic turbulence in a strong external magnetic field. *The Physics of Fluids*, 24(5):825–831, 1981.

D. Montgomery, M. R. Brown, and W. H. Matthaeus. Density fluctuation spectra in magnetohydrodynamic turbulence. *Journal of Geophysical Research*, 92(A1): 282–284, Jan 1987.

W. C. Müller and D. Biskamp. *The Evolving Phenomenological View on Magnetohydrodynamic Turbulence*. Springer Berlin Heidelberg, Berlin, Heidelberg, 2003. ISBN 978-3-540-36238-8.

N. J. Nelson, B. P. Brown, A. S. Brun, M. S. Miesch, and J. Toomre. Buoyant Magnetic Loops Generated by Global Convective Dynamo Action. *Solar Physics*, 289:441–458, Feb 2014.

Z. Němeček, J. Šafránková, O. Goncharov, L. Přech, and G. N. Zastenker. Ion scales of quasi-perpendicular low-Mach-number interplanetary shocks. *Geophysical Research Letters*, 40(16):4133–4137, Aug 2013.

K. W. Ogilvie, D. J. Chornay, R. J. Fritzenreiter, F. Hunsaker, J. Keller, J. Lobell, G. Miller, J. D. Scudder, Jr. Sittler, E. C., and R. B. Torbert. SWE, A Comprehensive Plasma Instrument for the Wind Spacecraft. *Space Science Reviews*, 71(1-4):55–77, Feb 1995.

E. N. Parker. Hydromagnetic Dynamo Models. *Astrophysical Journal*, 122:293, Sep 1955.

E. N. Parker. Dynamics of the Interplanetary Gas and Magnetic Fields. *Astrophysical Journal*, 128:664, Nov 1958.

E. N. Parker. *Interplanetary dynamical processes.* Interscience Publishers, New York, 1963.

G. K. Parks. *Physics of space plasmas - an introduction.* Redwood City, CA, Addison-Wesley Publishing Co., 1991.

G. Paschmann and P. W. Daly. Analysis Methods for Multi-Spacecraft Data. ISSI Scientific Reports Series SR-001, ESA/ISSI, Vol. 1. ISBN 1608-280X, 1998. *ISSI Scientific Reports Series*, 1, 1998.

J. H. Piddington. Solar Dynamo Theory and the Models of Babcock and Leighton. *Solar Physics*, 22(1):3–19, Jan 1972.

A. Pitňa, J. Šafránková, Z. Němeček, O. Goncharov, F. Němec, L. Přech, C. H. K. Chen, and G. N. Zastenker. Density Fluctuations Upstream and Downstream of Interplanetary Shocks. *Astrophysical Journal*, 819:41, Mar 2016.

A. Pitňa, J. Šafránková, Z. Němeček, L. Franci, L. Pi, and V. Montagud Camps. Characteristics of Solar Wind Fluctuations at and Below Ion Scales. *Accepted to Astrophysical Journal*, 2019.

A. Pitňa, J. Šafránková, Z. Němeček, and L. Franci. Decay of Solar Wind Turbulence behind Interplanetary Shocks. *Astrophysical Journal*, 844(1):51, Jul 2017.

J. J. Podesta. Radial decay law for large-scale velocity and magnetic field fluctuations in the solar wind. *Journal of Geophysical Research (Space Physics)*, 111(A8):A08103, Aug 2006.

J. J. Podesta. Dependence of Solar-Wind Power Spectra on the Direction of the Local Mean Magnetic Field. *Astrophysical Journal*, 698:986–999, Jun 2009.

J. J. Podesta. Evidence of Kinetic Alfvén Waves in the Solar Wind at 1 AU. *Solar Physics*, 286(2):529–548, Sep 2013.

E. Priest. *Magnetohydrodynamics of the Sun.* Cambridge University Press, 2014.

F. Pruneti and M. Velli. Parametric Decay of Large Amplitude Alfven Waves in the Solar Atmosphere. In A. Wilson, editor, *Fifth SOHO Workshop: The Corona and Solar Wind Near Minimum Activity*, volume 404 of *ESA Special Publication*, page 623, Jan 1997.

J. D. Richardson, K. I. Paularena, A. J. Lazarus, and J. W. Belcher. Radial evolution of the solar wind from IMP 8 to Voyager 2. *Geophysical Research Letters*, 22:325–328, Feb 1995.

O. W. Roberts, S. Toledo-Redondo, D. Perrone, J. Zhao, Y. Narita, D. Gershman, R. Nakamura, B. Lavraud, C. P. Escoubet, B. Giles, J. Dorelli, C. Pollock, and J. Burch. Ion-Scale Kinetic Alfvén Turbulence: MMS Measurements of the Alfvén Ratio in the Magnetosheath. *Geophysical Research Letters*, 45:7974–7984, Aug 2018.

L. Rudakov, M. Mithaiwala, G. Ganguli, and C. Crabtree. Linear and nonlinear Landau resonance of kinetic Alfvén waves: Consequences for electron distribution and wave spectrum in the solar wind. *Physics of Plasmas*, 18(1): 012307–012307, Jan 2011.

R. Z. Sagdeev and A. A. Galeev. *Nonlinear Plasma Theory*. Frontiers in Physics. W. A. Benjamin, Inc., 1969.

F. Sahraoui, M. L. Goldstein, P. Robert, and Y. V. Khotyaintsev. Evidence of a Cascade and Dissipation of Solar-Wind Turbulence at the Electron Gyroscale. *Physical Review Letters*, 102(23):231102, Jun 2009.

A. A. Schekochihin, A. B. Iskakov, S. C. Cowley, J. C. McWilliams, M. R. E. Proctor, and T. A. Yousef. Fluctuation dynamo and turbulent induction at low magnetic Prandtl numbers. *New Journal of Physics*, 9(8):300, Aug 2007.

A. A. Schekochihin, S. C. Cowley, W. Dorland, G. W. Hammett, G. G. Howes, E. Quataert, and T. Tatsuno. Astrophysical Gyrokinetics: Kinetic and Fluid Turbulent Cascades in Magnetized Weakly Collisional Plasmas. *The Astrophysical Journal Supplement*, 182:310–377, May 2009.

S. Servidio, W. H. Matthaeus, and P. Dmitruk. Depression of Nonlinearity in Decaying Isotropic MHD Turbulence. *Physical Review Letters*, 100(9):095005, Mar 2008.

S. Servidio, C. Gurgiolo, V. Carbone, and M. L. Goldstein. Relaxation Processes in Solar Wind Turbulence. *Astrophysical Journal*, 789(2):L44, Jul 2014.

J. V. Shebalin, W. H. Matthaeus, and D. Montgomery. Anisotropy in MHD turbulence due to a mean magnetic field. *Journal of Plasma Physics*, 29(3): 525–547, Jun 1983.

M. Shi, H. Li, C. Xiao, and X. Wang. The Parametric Decay Instability of Alfvén Waves in Turbulent Plasmas and the Applications in the Solar Wind. *Astrophysical Journal*, 842(1):63, Jun 2017.

C. W. Smith, K. Hamilton, B. J. Vasquez, and R. J. Leamon. Dependence of the Dissipation Range Spectrum of Interplanetary Magnetic Fluctuationson the Rate of Energy Cascade. *Astrophysical Journal*, 645:L85–L88, Jul 2006a.

C. W. Smith, B. J. Vasquez, and K. Hamilton. Interplanetary magnetic fluctuation anisotropy in the inertial range. *Journal of Geophysical Research (Space Physics)*, 111(A9):A09111, Sep 2006b.

C. W. Smith, B. J. Vasquez, and J. V. Hollweg. Observational Constraints on the Role of Cyclotron Damping and Kinetic Alfvén Waves in the Solar Wind. *Astrophysical Journal*, 745(1):8, Jan 2012.

I. V. Sokolov, I. I. Roussev, M. Skender, T. I. Gombosi, and A. V. Usmanov. Transport Equation for MHD Turbulence: Application to Particle Acceleration at Interplanetary Shocks. *Astrophysical Journal*, 696(1):261–267, May 2009.

S. R. Spangler and C. R. Gwinn. Evidence for an Inner Scale to the Density Turbulence in the Interstellar Medium. *Astrophysical Journal*, 353:L29, Apr 1990.

S. R. Spangler, J. A. Leckband, and I. H. Cairns. Observations of the parametric decay instability of nonlinear magnetohydrodynamic waves. *Physics of Plasmas*, 4(3):846–855, 1997.

T. Stribling and W. H. Matthaeus. Relaxation processes in a low-order three-dimensional magnetohydrodynamics model. *Physics of Fluids B: Plasma Physics*, 3(8):1848–1864, 1991.

J. Šafránková, Z. Němeček, L. Přech, G. Zastenker, I. Čermák, L. Chesalin, A. Komárek, J. Vaverka, M. Beránek, J. Pavlu, E. Gavrilova, B. Karimov, and A. Leibov. Fast Solar Wind Monitor (BMSW): Description and First Results. *Space Science Reviews*, 175:165–182, Jun 2013a.

J. Šafránková, Z. Němeček, L. Přech, and G. N. Zastenker. Ion Kinetic Scale in the Solar Wind Observed. *Physical Review Letters*, 110(2):025004, Jan 2013b. doi: 10.1103/PhysRevLett.110.025004.

J. Šafránková, Z. Němeček, F. Němec, L. Přech, A. Pitňa, C. H. K. Chen, and G. N. Zastenker. Solar Wind Density Spectra around the Ion Spectral Break. *Astrophysical Journal*, 803:107, Apr 2015.

J. Šafránková, Z. Němeček, F. Němec, D. Verscharen, C. H. K. Chen, T. Ďurovcová, and M. O. Riazantseva. Scale-dependent Polarization of Solar Wind Velocity Fluctuations at the Inertial and Kinetic Scales. *Astrophysical Journal*, 870:40, Jan 2019.

G.I. Taylor. The Spectrum of Turbulence. *Proc. R. Soc. London, Ser. A*, 164: 476–490, 1938.

J. M. TenBarge, J. J. Podesta, K. G. Klein, and G. G. Howes. Interpreting Magnetic Variance Anisotropy Measurements in the Solar Wind. *Astrophysical Journal*, 753(2):107, Jul 2012.

A. Tenerani and M. Velli. Parametric decay of radial Alfvén waves in the expanding accelerating solar wind. *Journal of Geophysical Research (Space Physics)*, 118(12):7507–7516, Dec 2013.

A. M. Title and C. J. Schrijver. The Sun's Magnetic Carpet. In R. A. Donahue and J. A. Bookbinder, editors, *Cool Stars, Stellar Systems, and the Sun*, volume 154 of *Astronomical Society of the Pacific Conference Series*, page 345, 1998.

C. Torrence and G. P. Compo. A Practical Guide to Wavelet Analysis. *BAMS*, 79:61–78, Jan 1998.

B. T. Tsurutani and G. S. Lakhina. Some basic concepts of wave-particle interactions in collisionless plasmas. *Reviews of Geophysics*, 35(4):491–501, 1997.

C.-Y. Tu and E. Marsch. MHD structures, waves and turbulence in the solar wind: Observations and theories. *Space Science Reviews*, 73:1–210, Jul 1995.

U. Villante. On the role of alfvénic fluctuations in the inner solar system. *Journal of Geophysical Research: Space Physics*, 85(A12):6869–6873, 1980.

G. L. Withbroe. The Solar Wind Mass Flux. *Astrophysical Journal*, 337:L49, Feb 1989.

H. Wu, D. Verscharen, R. T. Wicks, C. H. K. Chen, J. He, and G. Nicolaou. The Fluid-like and Kinetic Behavior of Kinetic Alfvén Turbulence in Space Plasma. *Astrophysical Journal*, 870:106, Jan 2019.

P. Wu, M. Wan, W. H. Matthaeus, M. A. Shay, and M. Swisdak. von Kármán Energy Decay and Heating of Protons and Electrons in a Kinetic Turbulent Plasma. *Physical Review Letters*, 111(12):121105, Sep 2013.

G. P. Zank, G. Li, V. Florinski, Q. Hu, D. Lario, and C. W. Smith. Particle acceleration at perpendicular shock waves: Model and observations. *Journal of Geophysical Research (Space Physics)*, 111(A6):A06108, Jun 2006.

J. S. Zhao, Y. Voitenko, M. Y. Yu, J. Y. Lu, and D. J. Wu. Properties of Short-wavelength Oblique Alfvén and Slow Waves. *Astrophysical Journal*, 793:107, Oct 2014.

Y. Zhou, W. H. Matthaeus, and P. Dmitruk. Colloquium: Magnetohydrodynamic turbulence and time scales in astrophysical and space plasmas. *Review of Modern Physics*, 76:1015–1035, Dec 2004.

List of Figures

List of Tables

List of author's publications

A. Pitňa, J. Šafránková, Z. Němeček, L. Franci, L. Pi, and V. Montagud Camps. Characteristics of Solar Wind Fluctuations at and Below Ion Scales. *Accepted to Astrophysical Journal*, 2019.

M. O. Riazantseva, V. P. Budaev, L. S. Rakhmanova, N. L. Borodkova, G. N. Zastenker, Y. I. Yermolaev, J. Šafránková, Z. Němeček, L. Přech, **A. Pitňa**. Intermittency of the solar wind density near the interplanetary shock. *Geomagnetism and Aeronomy*, 57(6):696–705, Nov 2017.

A. Pitňa, J. Šafránková, Z. Němeček, and L. Franci. Decay of solar wind turbulence behind interplanetary shocks. *Astrophysical Journal*, 844(1):51, Jul 2017.

A. Pitňa, J. Šafránková, Z. Němeček, O. Goncharov, F. Němec, L. Přech, C. H. K. Chen, and G. N. Zastenker. Density fluctuations upstream and downstream of interplanetary shocks. *Astrophysical Journal*, 819:41, Mar 2016.

J. Šafránková, Z. Němeček, F. Němec, L. Přech, **A. Pitňa**, C. H. K. Chen, and G. N. Zastenker. Solar wind density spectra around the ion spectral break. *Astrophysical Journal*, 803:107, Apr 2015.

O. Goncharov, J. Šafránková, Z. Němeček, L. Přech, **A. Pitňa**, G. N. Zastenker. Upstream and downstream wave packets associated with low-Mach number interplanetary shocks. *Geophysical Research Letters*, 41:8100–8106, Nov 2014

Papers attached to the thesis

A. Pitňa, J. Šafránková, Z. Němeček, L. Franci, L. Pi, and V. Montagud Camps. Characteristics of Solar Wind Fluctuations at and Below Ion Scales. *Accepted to Astrophysical Journal*, 2019.

A. Pitňa, J. Šafránková, Z. Němeček, and L. Franci. Decay of solar wind turbulence behind interplanetary shocks. *Astrophysical Journal*, 844(1):51, Jul 2017.

A. Pitňa, J. Šafránková, Z. Němeček, O. Goncharov, F. Němec, L. Přech, C. H. K. Chen, and G. N. Zastenker. Density fluctuations upstream and downstream of interplanetary shocks. *Astrophysical Journal*, 819:41, Mar 2016.